Precambrian Research 430 (2025) 107934

Contents lists available at ScienceDirect

Precambrian Research

journal homepage: www.elsevier.com/locate/precamres

Sedimentary model evolution and palaeoenvironmental significance of the Upper Ediacaran microbial dolomites

Yuan Zhou [a,b,c], Xuelian You [d], Qing Li [a,b,c,*], Zhuofeng Zhang [a,b,c], Qiang Du [a,b,c], Zhengyu Wei [a,b,c], Xinlong Li [a,b,c], Hui Zhou [e]

[a] Hainan Institute of China University of Petroleum (Beijing), Sanya 572075, China
[b] State Key Laboratory of Petroleum Resources and Engineering, China University of Petroleum (Beijing), Beijing 102249, China
[c] College of Geoscience, China University of Petroleum (Beijing), Beijing 102249, China
[d] School of Ocean Sciences, China University of Geosciences (Beijing), Beijing 100083, China
[e] Research Institute of Petroleum Exploration and Development, PetroChina, Beijing 100083, China

ARTICLE INFO

Keywords:
Ediacaran
Dengying Formation
Microbial dolomites
Sedimentary environment
Sedimentary evolution

ABSTRACT

Microbial dolomites are extensively developed in the upper Ediacaran Dengying Formation (*ca* 551.1 to 542.0 Ma) in the Sichuan Basin, China. However, these microbial dolomites underwent complex depositional processes, and their sedimentary environments remain debated. In this study, the petrographic, mineralogical, and geochemical characteristics of microbial dolomites in the upper Ediacaran Dengying Formation are systematically analyzed. The microbial dolomites (stromatolites, thrombolites, oncoids, botryoidal dolomites) in the upper Ediacaran Dengying Formation demonstrate the interplay between microbial activity and environmental conditions in a shallow restricted platform. Microbial structural diversity reflects hydrodynamic-microbial synergy: stromatolites and botryoidal dolomites are formed in low-energy, high-activity settings; dispersed thrombolites are formed under weak microbial influence; layered/reticular thrombolites and oncoids are developed via particle aggregation in high-energy environments. Two transgressive–regressive cycles correlate with "dolomite sea" events: the first driven by global climate (evaporation, localized anoxia), the second by tectonic uplift (Tongwan Movement I), underscoring tectonics' role in reservoir genesis. Geochemical indicators reflect post-glacial seawater stratification and weathering shifts, constraining environmental triggers for Ediacaran-Cambrian biotic complexity. Global comparisons reveal widespread microbial diagenesis during the Ediacaran, yet the Sichuan Basin exhibits unique tectono-climatic cyclicity. Although diagenesis obscures some geochemical signals, systematic analysis confirms the Dengying Formation as a critical archive for Precambrian carbonate factory evolution, microbial-environmental feedbacks, and early reservoir dynamics. This study advances understanding of late Precambrian Earth systems, bridging microbial processes, seawater chemistry, and tectono-climatic controls on carbonate preservation.

1. Introduction

The term microbialite was first introduced by Burne and Moore (1987), who defined it as sedimentary rocks formed by benthic microbial communities through trapping and binding of detrital sediments, or via inorganic or organic-induced mineralization associated with microbial activity. Microbialites are abundant in modern bioherm development and throughout geological history (Mei, 2007). The composition of microbialites is diverse and includes calcareous, iron-manganese, phosphatic, and siliceous materials, with microbial carbonates being the most common (Centeno et al., 2012). Microorganisms are among the earliest life forms on Earth. They emerged during the first 20 % of Earth's history and currently account for approximately 80 % of all life in the biosphere (Fischer and Knoll, 2006; Schieber, 2007). Moreover, they have significantly impacted the composition and structure of the atmosphere (Ehrlich, 1998). Therefore, the study of microbialites is crucial for reconstructing the paleoclimate and paleoenvironment.

Since the concept of microbialite was introduced, scholars have extensively studied their classification, formation mechanisms, controlling factors, ancient seawater chemistry, and their co-evolution with

* Corresponding author at: Hainan Institute of China University of Petroleum (Beijing), Sanya 572075, China.
E-mail addresses: zhouyuan@student.cup.edu.cn (Y. Zhou), liqing@cup.edu.cn (Q. Li).

https://doi.org/10.1016/j.precamres.2025.107934
Received 19 February 2025; Received in revised form 14 May 2025; Accepted 22 September 2025
Available online 29 September 2025

environments and organisms (Awramik, 1971; Dupraz et al., 2009; Dupraz and Visscher, 2005; Petrash et al., 2017; Wood et al., 2017). In recent decades, hydrocarbon-rich microbialite reservoirs have been identified in various regions worldwide. For example, the Ediacaran-Cambrian Ara Group in the South Oman Salt Basin has microbialite reservoirs with porosities reaching up to 17 %, with estimated recoverable reserves of approximately 18.8 billion barrels of oil (Al-Siyabi, 2005; Smodej et al., 2019). The Upper Jurassic Smackover Formation microbialite reservoirs in the Little Cedar Creek Field, located in the eastern Gulf of Mexico, have produced over 17.2 million barrels of oil (Mancini et al., 2004). In China, the Xiaoerbulake Formation in the Tarim Basin and the Leikoupo Formation in the Sichuan Basin have also been confirmed to possess significant exploration potential as microbialite reservoirs(He et al., 2019; Miao et al., 2024). These examples illustrate the high hydrocarbon generation potential of microbialites and serve as important hydrocarbon reservoirs.

In the Late Ediacaran period, thick microbial dolomite layers developed in the Dengying Formation of the Sichuan Basin, characterized by complex and diverse sedimentary features (Zhou et al., 2016). While recent studies have identified various facies types through detailed petrographic and stratigraphic analyses, there remains considerable debate regarding three key aspects of these microbial dolomites. First, classification criteria remain contentious, with some researchers emphasizing mesoscopic features, while others emphasize microscopic textures (Yan et al., 2022). Second, depositional models range from shallow-water platforms (Tan et al., 2022) to slope-tidal flat systems (Wang et al., 2006), with the proposed "dual-platform margin" model (Zhou et al., 2017) adding further complexity. Third, the genetic link between microbial activity and dolomite precipitation is still not well understood, as current interpretations often rely on indirect morphological evidence rather than process-specific geochemical tracers (Liu et al., 2024; Roberts et al., 2013). The diversity in interpretations highlights the need for a refined depositional framework.

The late Ediacaran microbial dolomite genesis and the associated seawater chemistry and paleoclimate characteristics remain subjects of ongoing debate in the geologic community (Chang et al., 2020; Cui et al., 2017). While some studies provide compelling evidence for microbial mediation in dolomite formation and the dolomite sea hypothesis, challenges persist in distinguishing microbial from abiotic processes and in reconstructing precise seawater characteristics (Li et al., 2021). For instance, although $\delta^{13}C_{VPDB}$ excursions are well documented (Liu et al., 2014), their interpretation as indicators of microbial metabolism versus global carbon cycle perturbations remains contentious (Li et al., 2021). Similarly, although rare earth element patterns are increasingly used to reconstruct seawater chemistry (Hu et al., 2020), their application in discriminating between syndepositional microbial signatures and later diagenetic overprints remains methodologically challenging.

In this study, the petrological, mineralogical, and geochemical characteristics of microbial dolomites in the Upper Ediacaran Dengying Formation in the central Sichuan Basin are systematically analyzed. The analysis integrates regional geology, sedimentary characteristics, tectonic evolution, and paleoceanographic conditions. This aims to clarify the classification and geochemical signatures. It also explores the depositional environment and the evolution of the Upper Ediacaran Dengying Formation. The objectives of this study are: (1) to develop a model that distinguishes microbial from environmental influences on dolomite textures; (2) to constrain the paleosalinity and redox conditions during dolomitization; and (3) to assess the interplay between tectonic events and global eustatic fluctuations in driving transgressive–regressive cycles. The integrated dataset provides new insights into how microbial communities interacted with Ediacaran seawater chemistry to produce these unique carbonate systems.

2. Geological setting

The Sichuan Basin, located in southwestern China, covers an area of approximately 260,000 km^2 and is part of the South China Block. It developed as a superimposed basin atop the Precambrian Yangtze Craton basement (Liu et al., 2021; Yao et al., 2011). The basin is bordered by mountain ranges and plateaus with elevations ranging from 2,000 to 3,000 m. Its margins are structurally controlled by tectonic belts including the Micang, Daba, Longmen, Liangshan, and Dalou mountains (Roger et al., 2010).

Tectonically, the Sichuan Basin lies within the stable interior of the Yangtze Block (Fig. 1A). Its evolution reflects the uplift–subsidence dynamics of the block, which can be divided into three major stages: (1) Neoproterozoic–Early Paleozoic intracratonic basin development, (2) Late Paleozoic–Early Mesozoic cratonic rifting, and (3) Late Triassic–Quaternary foreland basin formation and deformation (Merdith et al., 2017). Since the Ediacaran, the Yangtze Block entered a relatively stable platform stage. However, from the Ediacaran to the Early Cambrian, its sedimentary-tectonic evolution was influenced by cycles of continental breakup and amalgamation, producing significant uplift and subsidence (Li, 2003). U-Pb geochronology reveals temporal overlap (~551–541 Ma) between the development of the Dengying carbonate platform and the terminal phase of Rodinia breakup (~580–540 Ma), suggesting that the Sichuan Basin occupied a passive margin setting during this time (Yu et al., 2008). During deposition of the upper Ediacaran Dengying Formation to the Lower Cambrian Qiongzhusi Formation, the Yangtze Craton experienced the Tongwan Movement (~550–530 Ma), which encompassed three episodes of uplift and subsidence in the Upper Yangtze region (Li et al., 2015; Wang et al., 2014). The Tongwan tectonic phase includes three episodes of crustal uplift and subsidence affecting the Upper Yangtze region during the deposition of the Dengying and Maidiping formations (Wang, 2014). This tectonic phase is interpreted as a localized response to Rodinia's fragmentation. These tectonic dynamics strongly influenced the sedimentary systems of the central Sichuan Basin, where crustal extension produced localized subsidence centers and facilitated the development of widespread shallow marine carbonate platforms (Zhou et al., 2017).

The Ediacaran period spans ~ 635 to 541 Ma (Gradstein et al., 2004). The Doushantuo and Dengying Formations comprise the main Ediacaran sequence, with a boundary age of ~ 551 Ma (Condon et al., 2005). The Doushantuo Formation comprises mixed marine clastic–carbonate facies, while the Dengying Formation is characterized by thick microbial dolomites. Based on microbial content, the Dengying Formation can be divided into four lithological members (Fig. 1B) (Liu et al., 2021, 2013). Z_2dn^1 is mainly composed of muddy microcrystalline dolomite with local fine-crystalline dolomite, argillaceous dolomite, and microbial dolomite. Z_2dn^2 is characterized by thick microbial dolomites containing distinctive "botryoidal-lace shape" fabrics. Z_2dn^3 is a relatively thin unit of sandy to argillaceous dolomites, mudstones, and siltstones. Z_2dn^4 is rich in silica nodules and bands, primarily consisting of microbial dolomite, muddy microcrystalline dolomite, and siliceous dolomite.

During the Ediacaran Dengying period, the stable paleotectonic setting fostered the development of extensive shallow-marine environments (Liu et al., 2021). The Sichuan Basin was positioned in a low-latitude equatorial zone (Li et al., 2013). After the Sturtian and Marinoan glaciations (720–635 Ma), the climate became warmer and more humid, creating optimal conditions for microbial growth and facies development (Bowyer et al., 2023; Li et al., 2023a). During this time, depositional environments included shallow marine platforms, marginal seas, and localized restricted basins (Li et al., 2023b). Platform environments featured shallow waters, efficient water circulation, and low to moderate sedimentation rates. In the early Dengying Formation, the coexistence of carbonate platforms and rift basins facilitated the formation of the Upper Yangtze marginal platform, intraplatform rift zones, and the isolated platform system of the Central Yangtze region (Zhou et al., 2017). By the end of the Z_2dn^2 depositional stage, the Upper

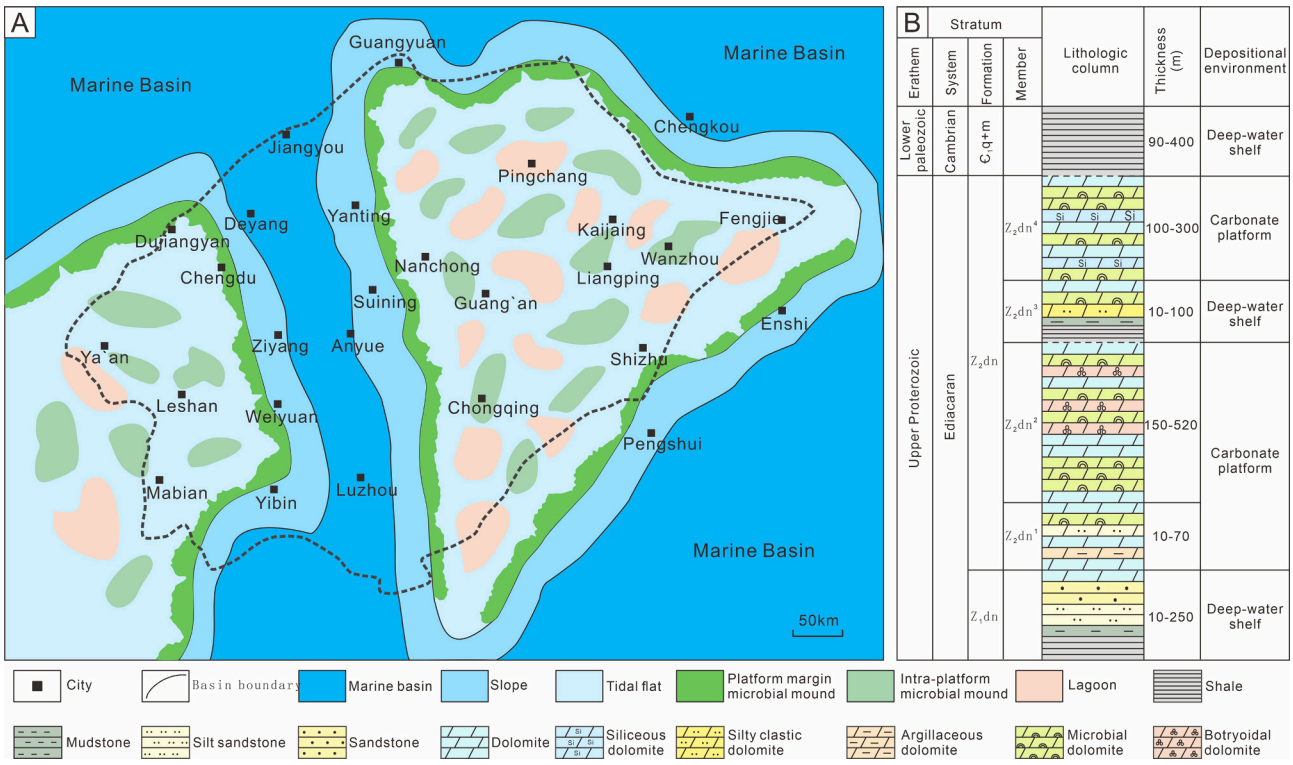

Fig. 1. Depositional setting and stratigraphic column of the Ediacaran Dengying Formation in the Sichuan Basin. (A) Paleogeographic map of the Dengying Formation (modified from Zhu et al., 2020). (B) Stratigraphic column of the Dengying Formation (modified from Zhang et al., 2014).

Yangtze region was uplifted by the Tongwan Movement I, leading to shallow marine shelf deposition atop an eroded paleotopographic landscape. During the Z_2dn^3 interval, rising sea levels triggered a transgression across the Central and Upper Yangtze regions (Li et al., 2012). The influx of significant terrigenous material hindered carbonate development, causing a transition of the sedimentary environment in both areas into a restricted marine setting dominated by terrigenous clastics (Liu et al., 2021). Z_2dn^4 is a continuation of Z_2dn^3, deposited during the highstand systems tract following the transgression, representing another significant phase of large-scale carbonate platform development (Tan et al., 2022).

3. Methods

The samples were collected from Well W117 in the central Sichuan Basin underwent petrological analyses, including core observation, optical microscopy, cathodoluminescence (CL), fluorescence microscopy (FL), and scanning electron microscopy (SEM). The optical microscopy, FL, and SEM observations were performed at the State Key Laboratory of China University of Petroleum (Beijing). CL analyses were conducted at the Beijing Institute of Nuclear Geology. Additionally, selected samples were analyzed for stable carbon and oxygen isotopic compositions, as well as trace and rare earth element concentrations.

3.1. Petrographic observation

The samples were polished to approximately 0.03 mm thickness for thin section observation and 0.1–0.2 mm thickness for CL and FL observations. The microscope used for thin section observation and FL microscopy was a model Nikon 50I-P100-L. CL observations were conducted using a Leica DM4500P polarized light microscope equipped with a CITL Mk5-2 cathodoluminescence component. CL images were captured under a vacuum pressure of 0.003 mbar, with a power supply voltage of 100–220 V (10A). The output voltage and current were set at 40 kV and 2 mA, respectively.

Fresh sample surfaces (~1 cm in both length and width) were coated with carbon to facilitate SEM testing. Samples were mounted onto the sample stage and appropriately labeled. They were placed in designated positions within the equipment, and a specific vacuum level was achieved. Examinations were conducted using a HITACHI S-4800 scanning electron microscope. The operating voltage was set to 10 kV, with a working distance of 8 mm.

3.2. Geochemistry examinations

Following detailed petrographic observations, dolomite samples unaffected by late-stage diagenesis were selected for micro-area sampling. The selected samples were ground to a powder finer than 200 mesh. Stable carbon and oxygen isotopes analyses were conducted using the 100 % phosphoric acid method with a MAT 253 mass spectrometer, reporting carbon and oxygen isotopes relative to the Vienna Pee Dee Belemnite (VPDB) standard. Powder samples (50 mg) were reacted with 100 % phosphoric acid at 50 °C under vacuum for 3 h to generate CO_2 gas. The C-O ratio of the equilibrated CO_2 gas was measured using a Finnigan MAT-253 mass spectrometer. The analytical precision was better than 0.1 %. The isotopic composition of dolomite was calculated using a phosphoric acid fractionation factor of 1.0093.

Trace and rare earth elements were quantified using inductively coupled plasma mass spectrometry (ICP-MS). Powder samples (50 mg) were weighed into a sealed digestion vessel, followed by the addition of 0.01 mL HF and 1.5 mL HNO_3. The vessels were placed in an oven and heated at 190 °C for 48 h. After cooling, the solution was concentrated to dryness at 140 °C, followed by the addition of 3 mL HCl and a second sealed digestion for 2 h. Following cooling, the extracted solution was transferred to PET bottles and sealed. Analyses were performed at a temperature of 23 °C with a relative humidity of 50.0 %. The experimental results exhibited an error margin of less than 2.0 %, well within the acceptable range. The obtained rare earth elements and yttrium (REY) mass fractions were normalized to Post-Archean Australian Shale (PAAS) (Mclennan, 2018). Standardized values are denoted by the

subscript "n" and were applied to calculate elemental anomalies using the following formula (Lawrence et al., 2006; Meyer et al., 2012):

$$Ce/Ce^* = Ce_n / (Pr_n^2/Nd_n)$$

$$Eu/Eu^* = Eu_n / (Sm_n^2 \times Tb_n)^{1/3}$$

$$Pr/Pr^* = 2Pr_n / (Ce_n + Nd_n)$$

4. Results

4.1. Types and characteristics of microbial dolomites

4.1.1. Stromatolite

Stromatolites are recognized as sedimentary structures formed through the trapping and binding of ions, debris, or particles, driven by microbial metabolic processes. Mesoscopically, the grain layers of stromatolites are nearly horizontal, exhibiting stable lateral extension or slight undulation (Fig. 2A). The layers are evenly spaced, with a thickness ranging from 0.5 mm to 1 mm, forming dense grain accumulations. Alternating bright and dark layers are present, with an overall grayish-white to grayish-black appearance. Under microscopic examination, the stromatolites are primarily composed of dark and light laminae (Fig. 2B, C, E). These laminae form the fundamental units, generally parallel to the bedding surfaces, with some areas exhibiting significant undulations. The dark laminae are predominantly composed of algal-rich materials, including algae, microbial detritus, and fine crystalline dolomite, with a thickness of 0.1 to 0.3 mm. The light laminae are composed of relatively larger dolomite crystals and range from 0.1 mm to 0.5 mm in thickness. Under CL (Fig. 2D), the dark laminae appear bright red, while the light laminae remain dark. FL reveals that the dark laminae exhibit strong fluorescence, whereas the light laminae show weak or negligible fluorescence (Fig. 2F). This fluorescence is attributed to the emission of specific wavelengths of light by organic matter when stimulated by an electron beam or excitation light. The bright appearance of dark laminae under both CL and FL suggests a high content of organic matter and the preservation of original organic materials.

4.1.2. Thrombolite

At the mesoscale (Fig. 3A, D, G), thrombolites resemble stromatolites in both shape and size, although they lack internal laminar structures. Microbial clots constitute the primary structural units of thrombolites, with clot, banded, and irregular morphologies. Microscopically, thrombolites are composed of irregular dark-grey pellets, clumps, and aggregated grains, with typical clot sizes ranging from 0.2 mm to 0.5 mm. Organic matter is concentrated around the clots, binding clay minerals, feldspathic detritus, and pyrite particles. Thrombolites are classified into three morphological types: dispersed, layered, and reticular thrombolites.

Mesoscopically, dispersed thrombolites appear as scattered spots (Fig. 3A). Microscopically, they display clot structures with limited content, weak inter-clot connectivity, and scattered distribution (Fig. 3B). Their lateral continuity is poor, and heterogeneity is pronounced. Individual clots are generally small (0.01–0.1 mm) and irregular in shape. Slightly larger clots occasionally form aggregates ranging from 0.1 mm to 0.3 mm. The internal cavities are small and irregular, with weak cementation and predominantly early-stage cement. Under CL, they appear mostly dark, indicating a low organic matter content (Fig. 3C).

Layered thrombolites exhibit discontinuous gray-white alternating layered structures (Fig. 3D). Microscopically, they display irregular banded structures formed by laterally elongated clots arranged directionally (Fig. 3E). These bands range from 0.3 mm to 0.8 mm in thickness and differ from stromatolitic laminae by their irregular shapes and variable thickness. The cavities between bands are filled with multi-generational cement composed of fine- to coarse-crystalline dolomite. Grain sizes increase from edge to center, ranging from 0.05 mm to 0.25 mm. Under CL, the clot bands appear bright red, while the dolomite in the cavities appears dark due to cementation (Fig. 3F).

Reticular thrombolites are characterized by a clot-grid structure (Fig. 3G). Their clot structures are densely packed and exhibit vertical growth trends, with a high abundance of clots. Microscopically, the clots aggregate into clumped structures ranging from 0.5 mm to 1 mm (Fig. 3H). These clots connect and coalesce, forming a three-dimensional network-like framework. Numerous large, irregularly distributed internal cavities are present. Fibrous cement lines the inner edges of these cavities in a ring-like structure, with a thickness of 0.1 mm to 0.2 mm. The interiors are filled with powder-crystalline dolomite (0.01–0.1 mm). Under CL, reticular thrombolites appear bright red, indicating the highest organic matter content among the three thrombolite types (Fig. 3I).

4.1.3. Oncoid

Oncoids generally appear dark and exhibit a grain-encrusted

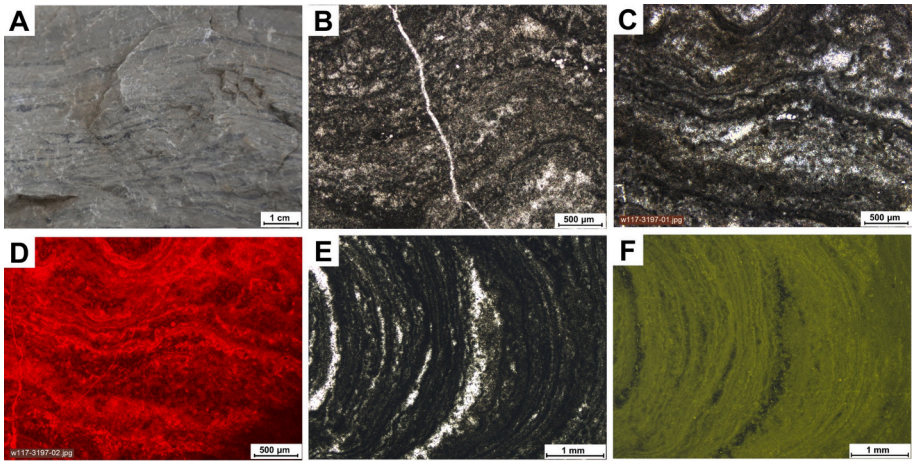

Fig. 2. Core and microscopic photographs of stromatolites. (A) Core photograph of stromatolite, straight layer structure, the gray-black layer is thin and the gray-white layer is thick, 3324.3 m. (B) Photomicrograph of stromatolite, corrugated dark and light laminae, 3197 m. (C) Photomicrograph of stromatolite, the upper half is corrugated laminae, and the lower half is straight laminae, 3197 m. (D) CL image of C, the dark laminae appear bright red, while the light laminae appear dark. (E) Photomicrograph of stromatolite, 3197 m. (F) FL image of E, the dark laminae appear bright, while the light laminae appear dark. (CL, cathodoluminescence; FL, fluorescence).

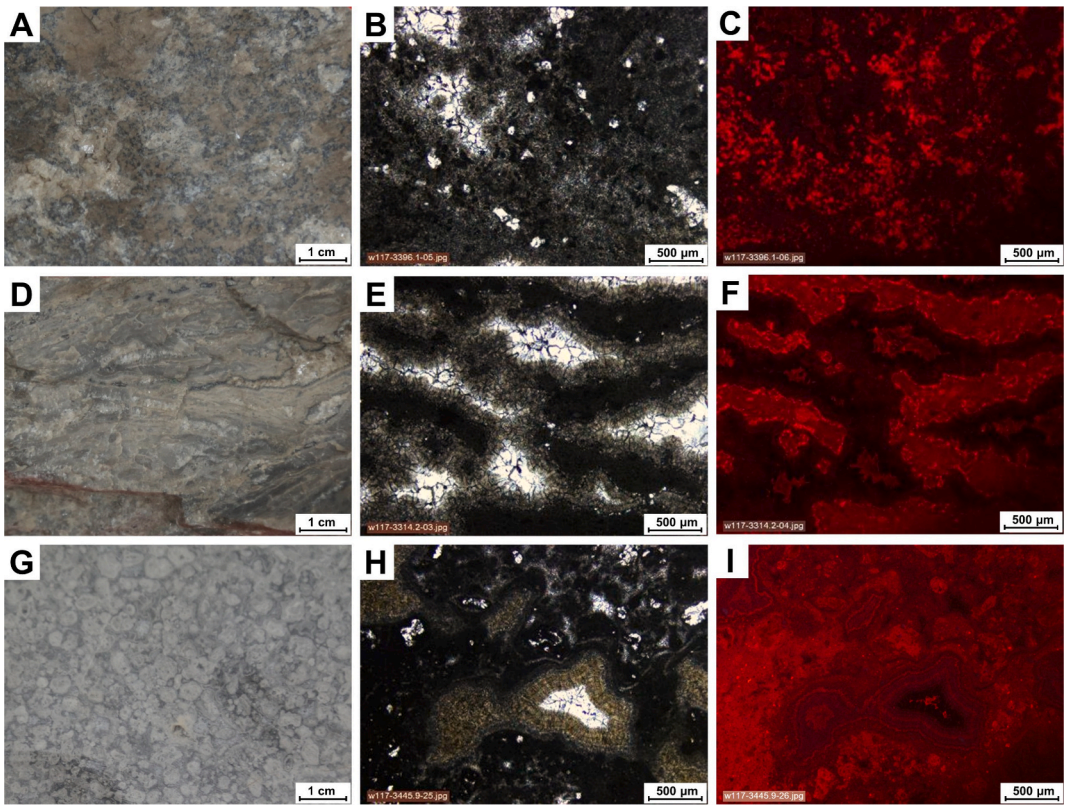

Fig. 3. Core and microscopic photographs of thrombolites. (A) Core photograph of dispersed thrombolite, spotted structure, 3314.2 m. (B) Photomicrograph of dispersed thrombolite, irregular clot structure with low clot content, 3396.1 m. (C) CL image of B, clots are bright red. (D) Core photograph of stratified thrombolite, discontinuous layered structure, 3366.3 m. (E) Photomicrograph of stratified thrombolite, irregular banded structures, 3314.2 m. (F) CL image of E, the clot bands are bright red. (G) Core photograph of gridded thrombolite, clot-grid structure, 3324.3 m. (H) Photomicrograph of gridded thrombolite, clots aggregate into clumped structures, 3445.9 m. (I) CL image of H, bright red with the most organic matter content.

structure (Fig. 4A). The core is typically composed of micritic clots, algal clumps, microbial fragments, or sand grains, ranging in size from 0.5 mm to 3 mm (Fig. 4B, D). The overall morphology of the oncoid shows a clear correlation with the shape of its core. As the encrustation layers accumulate, the thickness of the laminae increases, reducing the core's geometric influence (Tang, 2018). The encrustation typically forms concentric layers, which can be single-layered, multi-layered, or irregular. Similar to stromatolites, the encrustation is composed of dark algal-rich and light detrital-rich laminae. Oncoids mainly develop dark laminae, with thicknesses ranging from 0.05 mm to 0.3 mm. The light laminae are thin, with thicknesses ranging from 0.01 mm to 0.2 mm. As the oncoid grows, the laminae become progressively thicker. Under CL (Fig. 4C), the dark laminae exhibit bright red, while the light laminae appear dark. Under FL (Fig. 4E), the dark laminae exhibit bright yellow-green, whereas the light laminae exhibit no fluorescence.

4.1.4. Botryoidal dolomite

Botryoidal dolomites exhibit bead-like or botryoidal shapes in cross-section and laminar structures on the sides (Fig. 4F). They typically occur conformably with the bedding (Lin et al., 2017). They are mainly composed of core and surrounding encrustation (Fig. 4G). The core primarily consists of micritic dolomite or microbial structures, such as algal grains, algal clumps, or algal sand fragments. It typically exhibits irregular shapes and variable sizes, displaying both singular and composite forms, with diameters generally less than 5 mm. The surrounding encrustation is composed of alternating dark and light laminae arranged in parallel (Fig. 4H). The dark laminae consist of micritic or fibrous structures influenced by microbial processes. They are typically thin, resembling fine lines, with thicknesses ranging from 0.02 mm to 0.1 mm. The light laminae are primarily composed of fibrous dolomite, with crystals growing perpendicular to the bedding, and are generally thicker (from 0.1 mm to 2 mm). The fibrous crystals in each layer are consistent in form, exhibiting parallel and uniform thicknesses. Their growth remains continuous despite being separated by dark laminae. Under CL (Fig. 4I), alternating bands of red and dark red luminescence are observed, showing strong lateral continuity.

4.2. Mineral composition

The microbial dolomites primarily consist of dolomite, constituting 95 % of the mineral content. Based on their structural features, microbial dolomites can be classified into matrix dolomite (MD), fibrous dolomite (FD), and crystalline dolomite (CD). Minor amounts of calcite, ferroan dolomite, pyrite, apatite, quartz, and barite are also present.

Matrix dolomite (MD) exhibits a micritic to microcrystalline structure. Under the microscope, the grains are fine, less than 0.01 mm (Fig. 5A). The grain boundaries are indistinct, and crystal structures and morphologies, exhibiting subhedral to anhedral shapes, are difficult to identify. MD crystals are densely packed and contain filamentous or flocculent cryptoalgae and organic matter. Under CL (Fig. 5B), MD exhibits bright red, indicating high organic content and the preservation of original organic material. MD is commonly found within the dark laminae or clots of stromatolites, thrombolites, and oncoids.

Fibrous dolomite (FD) exhibits a fibrous-zoned structure (Fig. 5C-G). It forms after MD and grows perpendicular to the boundaries. Continuous horizontal bands are developed during growth, arranged in layers. The individual laminae range in thickness from 0.1 mm to 2 mm and are characterized by alternating light and dark laminae. The laminae may cross-cut existing layers during growth. FD grows outward perpendicular to the laminae, with little effect on the crystal structure, although

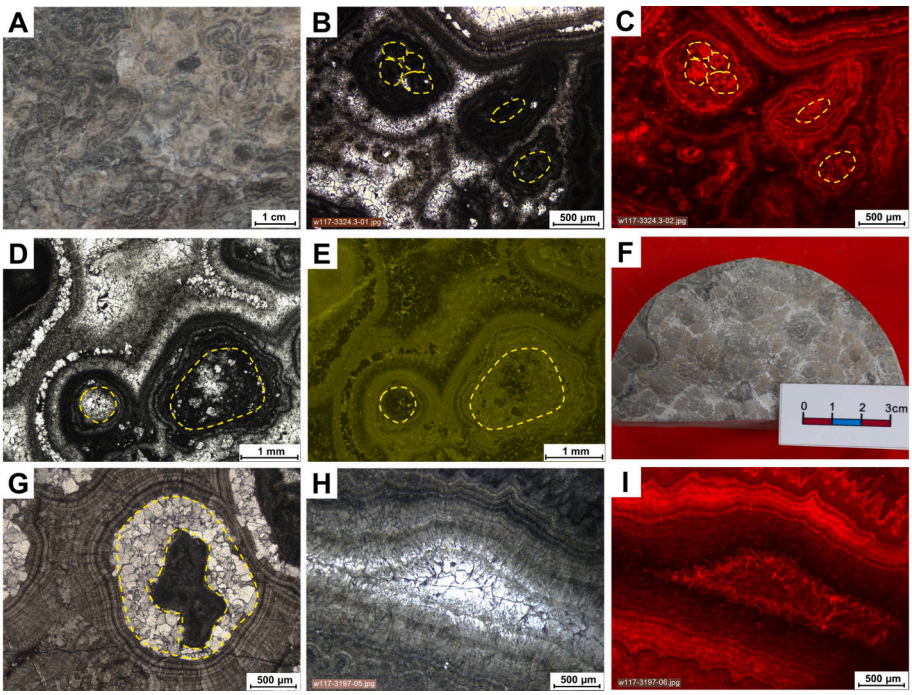

Fig. 4. Core and microscopic photographs of oncoids and botryoidal dolomites. (A) Core photograph of oncoid, grain-encrusted structure, 3363.9 m. (B) Photomicrograph of oncoid, composed of core and encrustation, 3324.3 m. (C) CL image of B, the core (yellow circle) and encrustation are bright red. (D) Photomicrograph of oncoid, part of the core is dissolved (yellow circle), 3324.3 m. (E) FL image of D, the core and encrustation have strong fluorescence. (F) Core cross-section photograph of botryoidal dolomite, bead-like or botryoidal shapes, 3324.12 m. (G) Photomicrograph of botryoidal dolomite, the core is strongly dissolved (yellow circle), and the encrustation develops fibrous zonal laminae, 3312 m. (H) Photomicrograph of botryoidal dolomite, fibrous structures, 3197 m. (I) CL image of H, bright and dark band structure.

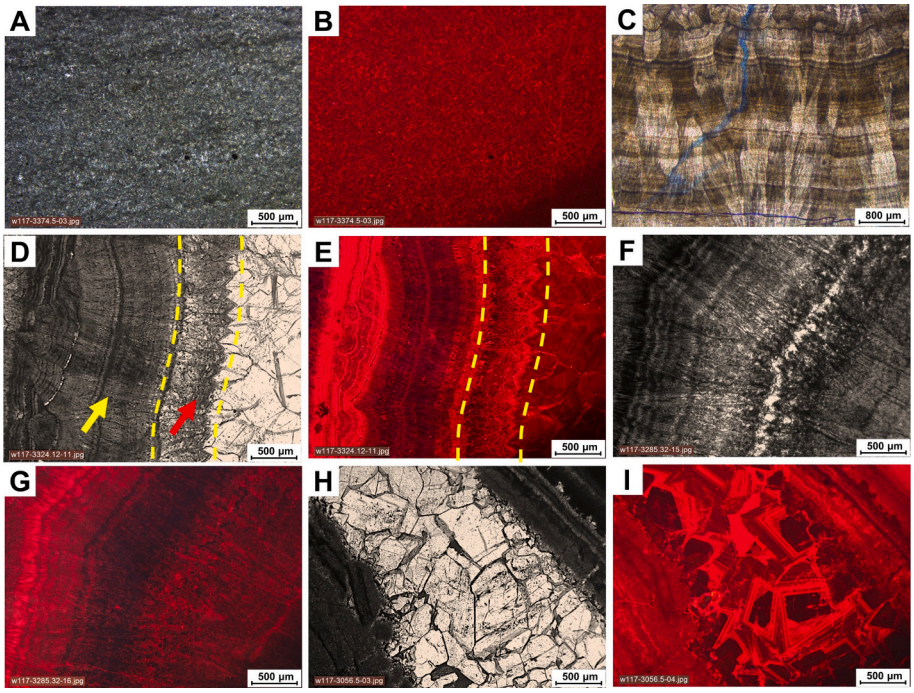

Fig. 5. Microscopic characteristics of microbial dolomites. (A) MD, micritic to microcrystalline structure, 3374.5 m. (B) CL image of A, bright red. (C) FD, fibrous-zoned structure, 3395.5 m. (D) FD, radiating fibrous structure (yellow arrow), foliated fibrous structure (red arrow), 3324.12 m. (E) CL image of D, well-preserved bands with alternating red and dark. (F) FD, foliated fibrous structure, 3285.3 m. (G) CL image of F, bright and dark band structure. (H) CD, euhedral to subhedral crystal structure, 3056.5 m. (I) CL image of H, multi-generation cemented zoned structure. (MD, matrix dolomite; FD, fibrous dolomite; CD, crystalline dolomite).

minor changes in laminae shape may occur due to growth direction. FD displays symmetry during growth. The bands on either side of the axis are symmetrical. Crystal sizes increase outward from the core, and the edges of the growth bands become indistinct, sometimes exhibiting radiating, rhomboidal, or foliated shapes. Under CL (Fig. 5E, G), FD shows well-preserved bands with alternating red and dark luminescence.

Crystalline dolomite (CD) exhibits large and bright crystals, ranging from 0.05 mm to 0.5 mm (Fig. 5H). These crystals are mainly euhedral to subhedral, though they may also form within a cavity. The crystals exhibit concavo-convex or interlocking contacts, with clearly defined grain boundaries. The crystal surfaces are relatively clean, though microfractures are common. Under CL (Fig. 5I), CD exhibits zoned structures, suggesting multi-generational cementation.

4.3. Microscopical characteristics of microbial dolomites

Under SEM, microbial dolomites display fine-grained textures, ranging from 0.5 μm to 5 μm (Fig. 6). Dolomite crystals generally appear as dark grey rhombic (Fig. 6A-B), with distinct crystal faces and edges. Their sizes vary from 1 μm to 6 μm and commonly form aggregates or veins. While most rhombic surfaces are smooth, some exhibit rough or irregular surfaces due to environmental factors during growth. In addition to rhombohedral forms, other morphologies such as spherical, ellipsoidal, filamentous, and irregular shapes are also present (Fig. 6C–H), all confirmed as dolomite by energy spectroscopy. Spherical dolomites range from 1 μm to 5 μm in size and occur either as isolated grains or in aggregates (Fig. 6C-E). Ellipsoidal crystals range from 5 μm to 10 μm (Fig. 6F). Filamentous dolomites have diameters ranging from 0.1 μm to 0.5 μm and lengths from 2 μm to 10 μm, often forming parallel or intertwined bundles (Fig. 6G-H). Extracellular polymeric substances (EPS) are associated with these structures (Fig. 6E-F). Pyrite is also commonly observed (Fig. 6I).

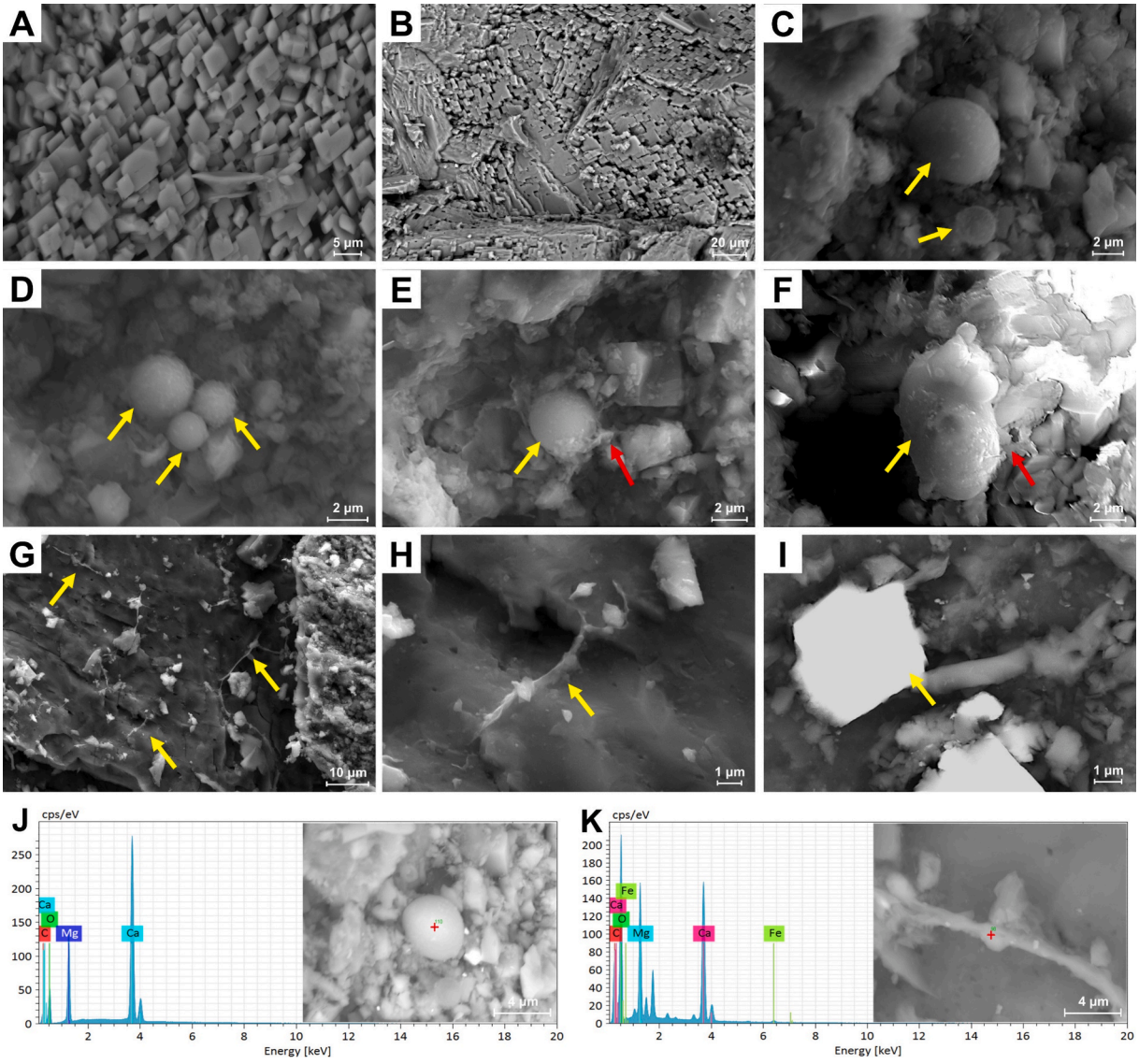

Fig. 6. Scanning electron microscope characteristics of microbial dolomites. (A-B) Rhombic dolomites, grain sizes ranging from 1 μm to 6 μm, 3017.8 m. (C-E) Spherical dolomites (yellow arrows), grain sizes ranging from 1 μm to 5 μm, 3418.2 m; EPS (red arrow), attached to spherical dolomite. (F) Ellipsoidal dolomite (yellow arrow), grain size ranging from 5 μm to 10 μm; EPS (red arrow), attached to ellipsoidal dolomite. (G-H) Filamentous dolomites, diameter ranging from 0.1 μm to 0.5 μm and length from 2 μm to 10 μm, 3395.5 m. (I) Pyrite (yellow arrow), grain size about 4 μm. (J) Spherical dolomite and its energy spectrum analysis spectra. (K) Filamentous dolomite and its energy spectrum analysis spectra.

Table 1
The C and O isotopic compositions, t and Z of microbial dolomites.

Lithology	Depth (m)	$\delta^{13}C_{VPDB}$ (‰)	$\delta^{18}O_{VPDB}$ (‰)	t (℃)	Z
Stromatolites	3430.1	2.2	−2.7	29.46	130.46
	3442.2	1.8	−3.4	32.95	129.29
	3502.4	2.1	−4.8	40.23	129.21
	3024	1.9	−3.9	35.50	129.25
	3041	2.2	−4.4	38.11	129.61
	3502.4	2.4	−3.5	33.46	130.47
Dispersed thrombolites	2997.2	3.3	−6.4	48.94	130.81
	3001.5	2.2	−4.6	39.00	129.58
	2992	1.2	−2.4	28.03	128.56
	3074	2.0	−4.0	35.77	129.43
	3087	1.5	−4.2	36.89	128.30
Layered thrombolite	3207	2.3	−6.5	49.60	128.77
	3184.8	1.1	−6.4	49.12	126.36
	3066	1.8	−7.3	53.92	127.47
	3462.3	1.0	−5.4	43.38	126.58
	3494.2	2.1	−4.9	40.69	129.17
Reticular thrombolites	3168.2	0.7	−7.8	56.95	124.84
	3472	1.5	−7.3	54.29	126.78
	3246.6	1.9	−5.1	41.84	128.65
	3284.6	1.2	−4.6	38.95	127.50
	3326.8	1.8	−6.8	51.56	127.61
Oncoids	3324.3	1.2	−6.3	48.46	126.62
	3417	1.7	−5.6	44.56	127.99
	3023	2.3	−6.4	49.03	128.82
	3324.3	1.9	−5.1	41.84	128.65
	3388.5	3.1	−5.9	46.22	130.71
	3388.5	1.3	−6.7	50.74	126.63
Botryoidal dolomites	3334.1	0.7	−8.4	60.75	124.55
	3171.8	1.5	−7.8	57.15	126.49
	3343.9	1.9	−7.9	57.74	127.26
	3137	1.0	−5.8	45.67	126.46
	3146.5	0.8	−7.2	53.62	125.35
	3285.32	1.1	−6.9	51.88	126.12
	3324.12	0.2	−7.9	57.74	123.78
	3318.5	1.8	−7.4	54.79	127.30

4.4. C and O isotopic compositions

The $\delta^{13}C_{VPDB}$ values of microbial dolomites range from 0.2 ‰ to 3.3 ‰, with an average of 1.7 ‰, and $\delta^{18}O_{VPDB}$ values from −8.4 ‰ to −2.4 ‰, averaging −5.7 ‰ (Table 1; Fig. 7). Stromatolites exhibit relatively enriched isotopic signatures, with $\delta^{13}C_{VPDB}$ values between 1.8 ‰ and 2.4 ‰ (average 2.1 ‰) and $\delta^{18}O_{VPDB}$ values from −4.8 ‰ to −2.7 ‰ (average −3.8 ‰). Thrombolites show $\delta^{13}C_{VPDB}$ of 0.7 ‰ to 3.3 ‰ (average 1.7 ‰) and $\delta^{18}O_{VPDB}$ values range from −7.8 ‰ to −2.4 ‰ (average −5.6 ‰). Dispersed thrombolites also show enrichment trends, with slightly lower $\delta^{13}C_{VPDB}$ values from 1.2 ‰ to 3.3 ‰ (average 2.0 ‰) and $\delta^{18}O_{VPDB}$ values from −6.4 ‰ to −2.4 ‰ (average −4.3 ‰). In contrast, layered thrombolites display relatively depleted isotopic values. The $\delta^{13}C_{VPDB}$ values range from 1.0 ‰ to 2.3 ‰ (average 1.7 ‰). The $\delta^{18}O_{VPDB}$ values range from −7.3 ‰ to −4.9 ‰ (average −6.1 ‰). The $\delta^{13}C_{VPDB}$ and $\delta^{18}O_{VPDB}$ values of reticular thrombolites are similar to those of layered thrombolites. The $\delta^{13}C_{VPDB}$ values range from 0.7 ‰ to 1.9 ‰ (average 1.4 ‰). The $\delta^{18}O_{VPDB}$ values range from −7.8 ‰ to −4.6 ‰ (average −6.3 ‰). Oncoids exhibit $\delta^{13}C_{VPDB}$ values of 1.2 ‰ to 3.1 ‰ (average 1.9 ‰) and $\delta^{18}O_{VPDB}$ values of −6.7 ‰ to −5.1 ‰ (average −6.0 ‰). Botryoidal dolomites show the most depleted trend, with $\delta^{13}C_{VPDB}$ values of 0.2 ‰ to 1.9 ‰ (average 1.1 ‰) and $\delta^{18}O_{VPDB}$ values of −8.4 ‰ to −5.8 ‰ (average −7.4 ‰).

4.5. Trace and REY compositions

Ni/Co ratios in microbial dolomites range from 2.183 to 7.870 (average 5.461). Specifically, stromatolites range from 4.000 to 6.000 (average 4.223), thrombolites from 2.972 to 7.733 (average 4.921), oncoids from 4.619 to 7.870 (average 5.865), and botryoidal dolomites from 6.310 to 7.714 (average 6.965) (Table 2). Sr/Ba ratios range from 0.738 to 3.299 (average 1.987). The Sr/Ba ratios for stromatolites, thrombolites, oncoids, and botryoidal dolomites range from 1.112 to 3.299 (average 2.446), 1.287 to 2.988 (average 2.184), 1.232 to 2.713 (average 1.940), and 0.738 to 1.571 (average 1.349) (Table 2). The $^{87}Sr/^{86}Sr$ ratios range from 0.7090 to 0.7101 (average 0.7095). The $^{87}Sr/^{86}Sr$ ratios for stromatolites, thrombolites, oncoids, and botryoidal dolomites range from 0.7093 to 0.7098 (average 0.7096), 0.7094 to 0.7101 (average 0.7097), 0.7092 to 0.7098 (average 0.7094), and 0.7090 to 0.7097 (average 0.7093) (Table 2).

Total REY concentrations are low, ranging from 0.069 ppm to 0.481 ppm (Table 2; Fig. 8A). Stromatolites, thrombolites, oncoids, and botryoidal dolomites have average ΣREY values of 0.212 ppm, 0.230 ppm, 0.154 ppm, and 0.151 ppm, respectively. Y/Ho ratio range from 34.222 to 95.857 (average 46.937) (Table 2; Fig. 8A). Ce and Eu anomalies range from 0.658 to 1.094 (average 0.883) and 0.719 to

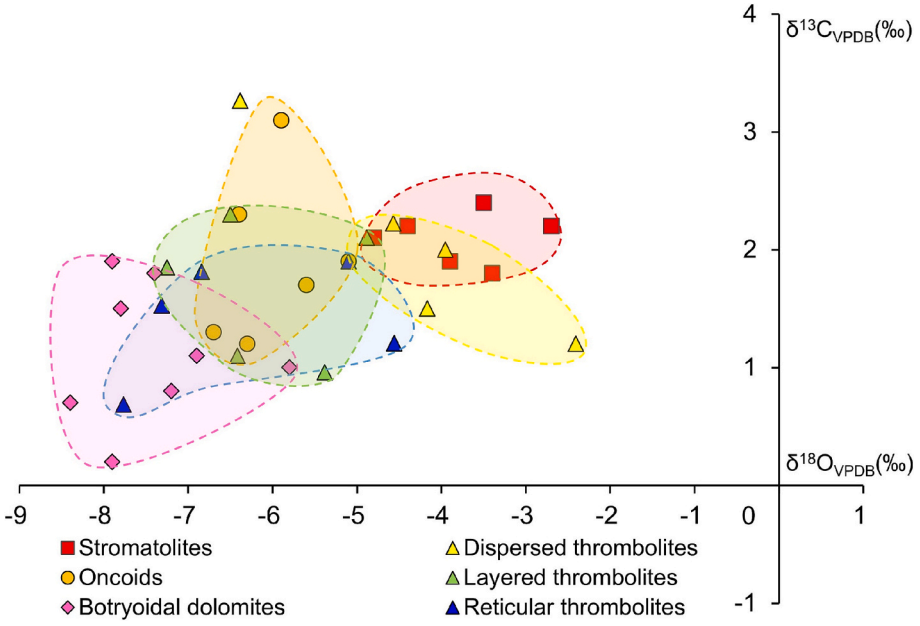

Fig. 7. Cross-plot of $\delta^{13}C_{VPDB}$ and $\delta^{18}O_{VPDB}$ of microbial dolomites.

Table 2
Trace and REY compositions of microbial dolomites (ICP-MS analytical uncertainty < 2 %).

Lithology	Depth (m)	La (ppm)	Ce (ppm)	Pr (ppm)	Nd (ppm)	Sm (ppm)	Eu (ppm)	Gd (ppm)	Tb (ppm)	Dy (ppm)	Y (ppm)	Ho (ppm)	Er (ppm)	Tm (ppm)	Yb (ppm)	Lu (ppm)
Stromatolites	3430.1	0.004	0.003	0.004	0.004	0.007	0.006	0.007	0.006	0.008	0.011	0.009	0.007	0.007	0.006	0.007
	3442.2	0.005	0.005	0.006	0.007	0.008	0.013	0.011	0.013	0.013	0.014	0.008	0.010	0.010	0.008	0.007
	3491.4	0.008	0.008	0.010	0.010	0.015	0.031	0.015	0.021	0.020	0.025	0.019	0.017	0.020	0.019	0.016
	3502.4	0.008	0.004	0.006	0.006	0.009	0.012	0.007	0.009	0.007	0.010	0.006	0.007	0.005	0.004	0.006
Thrombolites	3016.5	0.010	0.007	0.009	0.010	0.014	0.025	0.014	0.018	0.018	0.035	0.019	0.019	0.017	0.017	0.023
	3216.0	0.014	0.014	0.019	0.022	0.035	0.056	0.033	0.041	0.037	0.049	0.035	0.028	0.025	0.021	0.025
	3131.8	0.010	0.009	0.011	0.013	0.019	0.022	0.017	0.022	0.017	0.030	0.018	0.017	0.017	0.016	0.021
	3263.9	0.016	0.013	0.016	0.018	0.022	0.024	0.023	0.025	0.022	0.032	0.022	0.021	0.015	0.021	0.018
	3245.9	0.008	0.006	0.006	0.007	0.008	0.013	0.009	0.009	0.008	0.010	0.006	0.006	0.007	0.005	0.005
	3372.3	0.023	0.017	0.018	0.019	0.021	0.031	0.027	0.031	0.028	0.030	0.022	0.026	0.022	0.022	0.021
	3425.2	0.016	0.016	0.021	0.024	0.038	0.044	0.037	0.045	0.040	0.050	0.036	0.030	0.032	0.027	0.025
	3056.5	0.008	0.006	0.007	0.008	0.011	0.019	0.011	0.016	0.016	0.028	0.017	0.017	0.015	0.021	0.023
Oncoids	3324.3	0.011	0.008	0.009	0.009	0.016	0.021	0.014	0.018	0.017	0.019	0.012	0.014	0.012	0.008	0.009
	3088.5	0.010	0.008	0.009	0.009	0.010	0.017	0.011	0.016	0.015	0.016	0.012	0.011	0.012	0.008	0.009
	3352.5	0.010	0.008	0.008	0.008	0.013	0.020	0.012	0.014	0.013	0.015	0.011	0.010	0.012	0.006	0.007
	3395.5	0.003	0.003	0.003	0.003	0.005	0.009	0.005	0.006	0.004	0.006	0.004	0.005	0.013	0.003	0.005
Botryoidal dolomites	3171.8	0.010	0.010	0.010	0.011	0.017	0.031	0.021	0.023	0.024	0.050	0.024	0.023	0.037	0.029	0.028
	3166.0	0.016	0.016	0.017	0.019	0.030	0.053	0.028	0.041	0.037	0.064	0.030	0.031	0.032	0.032	0.032
	3285.3	0.009	0.012	0.009	0.006	0.014	0.015	0.016	0.021	0.019	0.032	0.020	0.018	0.020	0.017	0.016
	3324.1	0.004	0.005	0.004	0.002	0.009	0.010	0.005	0.009	0.009	0.014	0.008	0.008	0.007	0.008	0.012
	3318.5	0.002	0.004	0.004	0.004	0.007	0.011	0.007	0.010	0.010	0.009	0.008	0.006	0.006	0.004	0.005

Lithology	Depth (m)	Sr (μg /g)	Ba (μg /g)	Co (μg /g)	Ni (μg /g)	$^{87}Sr/^{86}Sr$	Sr/Ba	Ni/Co	∑REY (ppm)	LREY /HREY	Y/Ho	Ce/Ce*	Eu/Eu*	$(Dy/Sm)_n$	$(La/Sm)_n$	$(Nd/Yb)_n$
Stromatolites	3430.1	48.5	43.6	0.2	1.1	0.7096	1.112	6.000	0.098	0.499	37.222	0.802	0.965	1.123	0.566	0.728
	3442.2	36.8	15.0	0.1	0.6	0.7093	2.453	4.708	0.136	0.537	48.500	0.863	1.433	1.694	0.650	0.851
	3491.4	53.4	18.3	21.8	47.6	0.7098	2.918	2.183	0.254	0.559	39.053	0.902	1.805	1.311	0.544	0.548
	3502.4	50.8	15.4	2.1	8.3	0.7097	3.299	4.000	0.106	0.901	46.000	0.789	1.352	0.799	0.925	1.633
Thrombolites	3016.5	47.8	16.0	0.2	0.9	0.7099	2.988	3.905	0.257	0.508	49.632	0.930	1.649	1.325	0.749	0.577
	3216.0	49.3	19.1	0.4	1.9	0.7101	2.581	4.796	0.455	0.648	38.000	0.863	1.539	1.075	0.414	1.032
	3131.8	54.7	34.8	0.3	2.3	0.7095	1.572	7.733	0.258	0.582	44.389	0.960	1.118	0.892	0.515	0.818
	3263.9	47.1	36.6	2.7	11.7	0.7097	1.287	4.415	0.310	0.657	39.273	0.923	1.050	0.983	0.729	0.869
	3245.9	48.6	19.3	5.9	19.2	0.7100	2.518	3.254	0.112	0.878	43.333	0.926	1.519	0.928	0.992	1.264
	3372.3	49.5	22.4	1.2	9.1	0.7095	2.210	7.484	0.356	0.648	36.409	0.950	1.289	1.341	1.094	0.868
	3425.2	47.6	23.2	2.1	10.2	0.7096	2.052	4.811	0.481	0.581	37.222	0.857	1.084	1.062	0.422	0.908
	3056.5	34.2	15.1	1.8	5.4	0.7094	2.265	2.972	0.222	0.430	44.765	0.836	1.502	1.497	0.684	0.393
Oncoids	3324.3	47.3	38.4	2.3	18.1	0.7094	1.232	7.870	0.198	0.712	42.083	0.997	1.257	1.056	0.677	1.147
	3088.5	52.9	19.5	0.4	1.9	0.7098	2.713	4.619	0.173	0.675	36.917	0.877	1.431	1.440	1.038	1.118
	3352.5	51.0	31.7	0.1	0.6	0.7092	1.609	6.286	0.169	0.780	36.455	0.924	1.523	1.021	0.761	1.314
	3395.5	44.6	20.2	0.3	1.2	0.7093	2.208	4.685	0.077	0.577	40.500	0.848	1.844	0.901	0.726	0.989
Botryoidal dolomites	3171.8	55.8	35.5	0.1	0.7	0.7094	1.572	7.714	0.347	0.424	50.250	1.070	1.656	1.367	0.570	0.372
	3166.0	56.5	39.9	0.1	0.8	0.7095	1.416	6.310	0.479	0.570	51.667	1.091	1.571	1.214	0.539	0.582
	3285.3	42.6	28.2	0.1	0.6	0.7091	1.511	7.038	0.244	0.448	43.650	1.068	0.919	1.321	0.651	0.380
	3324.1	37.5	50.8	0.8	5.8	0.7090	0.738	7.332	0.114	0.512	47.125	1.060	1.062	0.996	0.436	0.318
	3318.5	21.6	14.3	0.9	5.7	0.7097	1.510	6.431	0.098	0.569	48.125	1.104	1.366	1.358	0.352	0.904

2.797 (average 1.444) (Table 2; Fig. 8B). The $(Dy/Sm)_n$ and $(La/Sm)_n$ ratios range from 0.327 to 1.694 (average 1.090) and 0.400 to 2.029 (average 0.842) (Table 2; Fig. 8C-D). The $(Nd/Yb)_n$ and LREY/HREY ratios range from 0.393 to 1.966 (average 1.058) and 0.423 to 1.741 (average 0.740) (Table 2; Fig. 8E).

5. Discussion

5.1. Sedimentary environments of microbial dolomites

Microbial dolomite is formed through the combined influence of microbial communities and sedimentary environments (Zhu and Dittrich, 2016). The spheroidal and filamentous structures observed under SEM strongly resemble those of modern and fossilized microbial structures, particularly cyanobacteria (Fig. 6C–H). These structures have been confirmed as dolomite by SEM energy spectrum analysis (Fig. 6J-K). Although these features are consistent with microbial influence, diagenetic overprinting cannot be entirely excluded (Yuan et al., 2022). Similar textural features have been reported in Ediacaran–Cambrian dolomites from the Ara Group in Oman (Wood et al., 2023) and the Lower Cambrian carbonates of the Tarim Basin (Jiang et al., 2021), where microbial mediation is supported by microfabric, isotopic, and mineralogical evidence. These analogues reinforce the interpretation that microbial processes can strongly influence early dolomite precipitation.

However, abiotic mechanisms cannot be excluded. Dolomite with similar morphologies may also form under purely physico-chemical conditions, such as direct precipitation in evaporitic environments or through dolomitization driven by organic matter degradation in the absence of microbial catalysts (Hu, 2019; Manche and Kaczmarek, 2019; Roberts et al., 2013). In particular, early diagenetic dolomite can display spheroidal forms due to supersaturation and localized geochemical gradients (Vandeginste et al., 2023). To address these possibilities, stable carbon isotope measurements were integrated. The $\delta^{13}C_{VPDB}$ values of the dolomite phases are within the typical range of microbial carbonate precipitation (−5 to + 5 ‰) (Bosak et al., 2013; Schidlowski, 1988). Although abiotic processes may have contributed to early dolomitization, microbial activity played a dominant role in dolomite precipitation.

The development of pyrite has been interpreted as evidence for sulfate reduction reactions (Fig. 6I) (Braissant et al., 2003). The metabolic activity of sulfate-reducing bacteria has been shown to influence and regulate microbial dolomite precipitation (Jiang et al., 2024). In addition, EPS with different morphologies have been observed

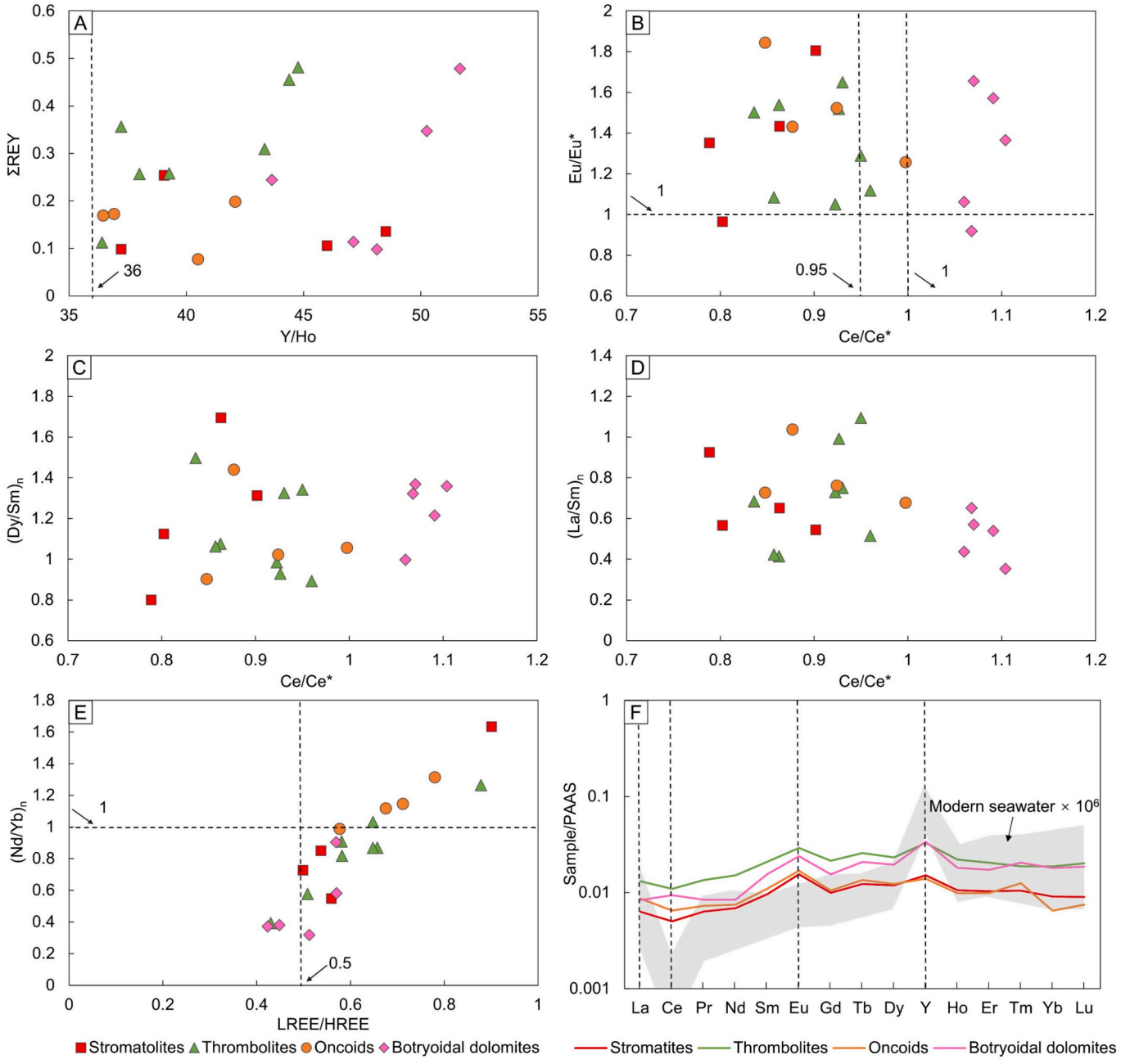

Fig. 8. Cross-plots of various elements and parameters. (A) Y/Ho ratio against ΣREY for terrestrial materials effects. (B-D) Ce/Ce* against Eu/Eu*, $(Dy/Sm)_n$, and $(La/Sm)_n$ for the influence of late diagenesis. (E) LREE/HREE against $(Nd/Yb)_n$ for the degree of differentiation of rare earth elements. (F) The average normalized REY patterns of microbial dolomites.

surrounding dolomite crystals under SEM (Fig. 6E-F). The high viscosity of EPS enables them to tightly bind sediment particles, thereby forming a solid matrix (Hartley et al., 1996). These matrices provide favorable conditions for microbial communities to attach to the debris particles and develop microbial mats. The presence of microbial mats further provides stable ecological conditions for microbial survival and metabolism (Robles-Fernández et al., 2022). The synergistic interactions between microorganisms and the environment are crucial for microbial capture, sediment binding, self-mineralization, and primary dolomite precipitation, which are essential for dolomite formation (Bernhard et al., 2023). During this process, microbial trapping and binding aggregate tiny particles in the water into sedimentary structures strongly influenced by hydrodynamic conditions and microbial activity (Fig. 10A). In low-energy environments with strong microbial activity, sediment particles settle steadily, forming laminar structures dominated by stromatolites and botryoidal dolomites. In environments with weak microbial activity, continuous lamination is less likely to form, and the lithology predominantly consists of dispersed thrombolites. In high-energy environments, particles form compact clotted structures or concentric spherical laminations, with lithology dominated by layered thrombolites, reticular thrombolites, and oncoids.

The formation of stromatolite laminae requires a relatively stable sedimentary environment. This process typically occurs in supratidal or upper intertidal zones (Fig. 9), facilitating the continuous development of microbial mats and gradual sediment accumulation (Lee and Riding, 2023). Hydrodynamic conditions significantly influence both the formation and morphology of stromatolites (Li et al., 2021). In low-energy environments, the limited transport of sediments promotes stromatolite

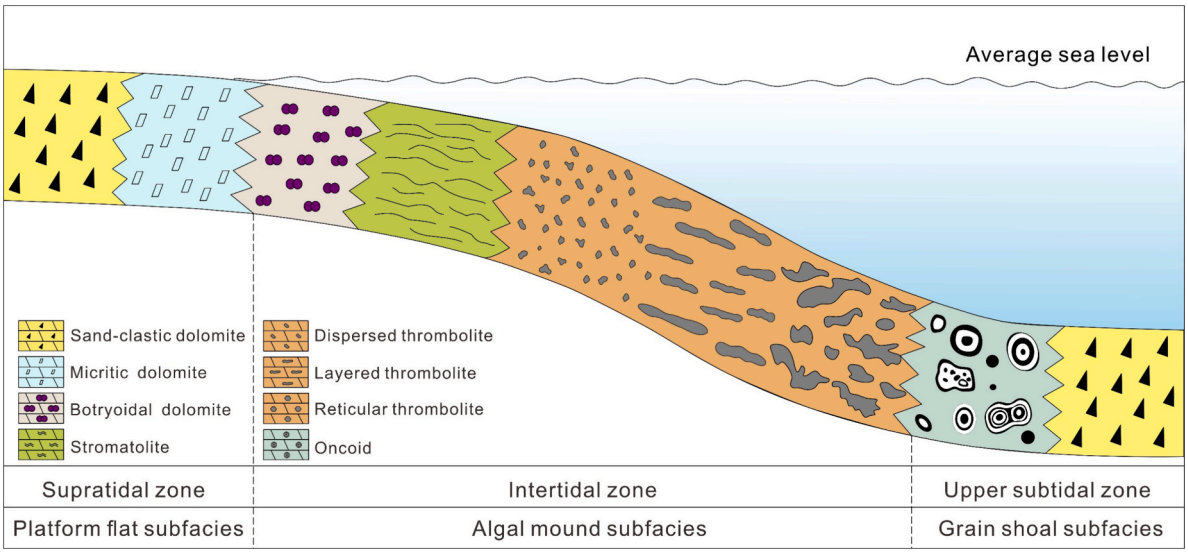

Fig. 9. Sedimentary facies distribution of microbial dolomites.

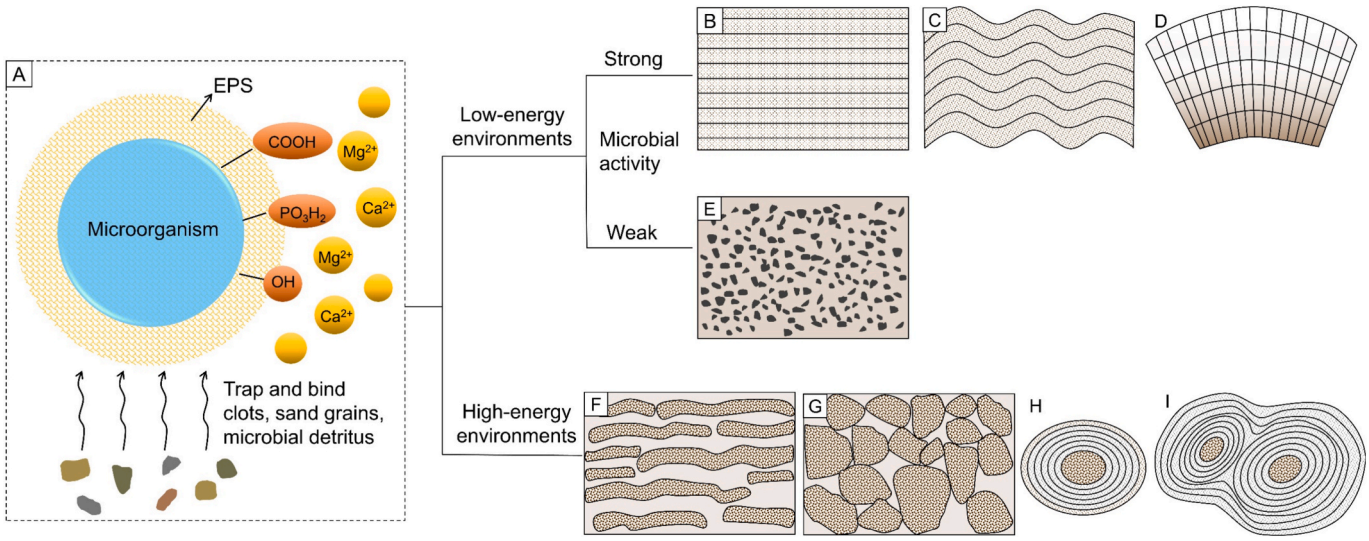

Fig. 10. Different microbial dolomite structures formed by microbial communities. (A) Microbial trapping and binding process. (B) Straight stromatolite. (C) Corrugated stromatolite. (D) Botryoidal dolomite. (E) Dispersed thrombolite. (F) Layered thrombolite. (G) Reticular thrombolite. (H) Simple oncoid. (I) Compound oncoid.

growth, resulting in the development of straight laminae (Fig. 10B). In environments with moderate hydrodynamic conditions, corrugated laminae are developed (Fig. 10C). In high-energy environments, strong water flow may disrupt microbial mat and thereby hinder stromatolite development (Awramik, 1971).

Thrombolites are primarily deposited in intertidal to upper subtidal zones characterized by strong hydrodynamics (Sun et al., 2021). Dispersed thrombolites are primarily distributed in low-energy lower supratidal and upper intertidal zones (Fig. 9). In these environments, microbial communities grow freely, forming small spherulitic structures without requiring binding to resist wave action (Bernhard et al., 2023). Microbial populations in thrombolites are less abundant, thereby preventing the development of continuous lamination (Xiao et al., 2019). The small size and sparse distribution of clots hinder the construction of a supportive framework, leading to fewer cavities (Fig. 10E). Layered thrombolites are developed in high-energy intertidal zones (Figs. 9, 10F). Their formation is attributed to vertical thickening and lateral expansion of microbial mats (Bernhard et al., 2023). Light availability may influence the growth of banded structures. In deep waters with limited light, microbes may grow vertically while extending laterally to optimize photosynthesis (Dupraz et al., 2009). Reticular thrombolites are formed in more dynamic lower intertidal and subtidal zones (Fig. 9). They form a supportive and wave-resistant gridding structure through vertical trapping and banding (Fig. 10G). Through microbial biostability, sediment integrity is maintained under high-energy conditions, thereby minimizing subsequent erosion (Paul et al., 2021). Clots are enclosed by micritic cement, enhancing preservation and producing darker coloration (Chacón-Baca et al., 2024).

Oncoids are formed in lower intertidal and subtidal zones where hydrodynamic conditions are intense (Fig. 9). Favorable hydrodynamic conditions facilitate oncoids transport and deposition (Xiao et al., 2020a). The core is transported by rolling or hopping under hydrodynamic forces (Riaz et al., 2022). Algae and microorganisms proliferate around the core, facilitating the trapping and binding of sediment particles into concentric laminae (Diaz et al., 2017). As sediment accumulates, oncoids evolve into spherical or ellipsoidal forms (Fig. 10*H*). Their

increased size eventually limits further transport (Xiao et al., 2020b). Oncoids continue to grow vertically while the lower laminae remain undeveloped. Intermittent rolling results in the formation of irregular concentric laminae (Dahanayake, 1978). Under active hydrodynamic conditions, small oncoids may coalesce and bond, becoming encased in sediment to form compound oncoids with multiple cores (Fig. 10I). Compound oncoids are typically larger than simple oncoids (Tang, 2018).

Botryoidal dolomites are typically formed in the lower supratidal to upper intertidal zones (Fig. 9). Their cores are formed during the syngenetic phase through seawater deposition and microbial trapping and binding (Zhai et al., 2020). Subsequent exposure and dissolution of the platform result in fractures and pores. These are then permeated by saturated carbonate solutions generated through seawater evaporation or mixing with meteoric water (Hu et al., 2020). Microbial activity promotes dolomite precipitation, with crystals growing radially outward from the core or perpendicularly from sediment surfaces, forming fibrous structures (Song et al., 2024). Continued sedimentation and crystal growth eventually produce the laminated architecture characteristic of botryoidal dolomites (Fig. 10D) (Wang et al., 2020; Zhang et al., 2022a).

5.2. Preservation of primary seawater chemical signals

The REY in marine carbonates are widely recognized as indicators of REY distribution in ancient seawater and are valuable for reconstructing the physicochemical conditions of seawater during carbonate formation (Webb and Kamber, 2000). REY values often indicate contributions from multiple sources, including seawater, detrital inputs, hydrothermal activity, and diagenetic processes (Bi et al., 2021). During carbonate deposition, silicate detritus rich in REY may be incorporated. Even small amounts of silicate detritus dissolved during the experimental process can alter the REY characteristics of the carbonates, potentially affecting the interpretation of the redox conditions of the original seawater (Ling et al., 2013). The REY values reported here (ranging from 0.062 ppm to 0.481 ppm) are significantly lower than the average REY content of terrigenous detritus (average 100 ppm) (Table 2, Fig. 8A). This suggests that the microbial dolomites were minimally affected by terrigenous materials during both deposition and subsequent diagenesis. Thus, the microbial dolomites effectively preserve the geochemical characteristics of ancient seawater REY.

There is a marked difference in the Y/Ho ratio between terrigenous sediments and marine carbonates, rendering this ratio an effective indicator for differentiating marine from non-marine deposits (Bau and Dulski, 1996). When the Y/Ho ratio exceeds 36, the REY in carbonates is interpreted as reflecting the signature of original seawater (Ling et al., 2013). All the samples analyzed exhibit Y/Ho ratios exceeding 36 (Table 2, Fig. 8A). They can be interpreted as representing the original seawater depositional environment. Diagenesis can alter the partitioning pattern of REY, typically resulting in enrichment of Ce, depletion of Eu, and reductions in the $(Dy/Sm)_n$ and $(La/Sm)_n$ ratios (Shields and Stille, 2001). Therefore, if negative correlations are observed between Ce/Ce*, Eu/Eu*, $(Dy/Sm)_n$, and $(La/Sm)_n$, this would suggest diagenetic modification of the REY distribution. In the samples, no significant negative correlations were observed between these parameters (Fig. 8B-D), implying minimal influence of diagenetic alteration on the samples. The data are robust for paleoenvironmental analysis.

During carbonate formation, temperature influences the oxygen isotopic composition, changing by approximately 2.6 ‰ per °C, while the effect on the carbon isotopic composition is comparatively minor, at only 0.035 ‰ per °C (Emrich et al., 1970). Therefore, variations in $\delta^{18}O_{VPDB}$ can serve as indicators of paleotemperature trends during carbonate rock diagenesis. The paleotemperature can be estimated using the following equation (Shackleton and Kennett, 1976, p. 281):

$$t = 16.9 - 4.38\left(\delta^{18}O_C - \delta^{18}O_W\right) + 0.1\left(\delta^{18}O_C - \delta^{18}O_W\right)^2$$

In the formula, t represents the paleoseawater temperature of carbonate rock formation; $\delta^{18}O_C$ represents the $\delta^{18}O_{VPDB}$ value measured in carbonate; $\delta^{18}O_W$ represents the $\delta^{18}O_{VPDB}$ value of paleoseawater. The $\delta^{18}O_{VPDB}$ values of seawater before the Cenozoic remain undetermined. It is generally assumed to be 0, similar to present-day values (Galili et al., 2019). Based on this formula, the temperature of the samples ranges from 28.03 °C to 60.75 °C, with an average of 45.68 °C (Table 1, Fig. 11A). These values are roughly consistent with those reported in previous studies and align with the suitable conditions for microbial proliferation (Knauth, 2005; Meng et al., 2011; Robert and Chaussidon, 2006). The temperature range for stromatolites, thrombolites, oncoids, and botryoidal dolomites is 29.46 °C to 40.23 °C (average 34.95 °C), 28.03 °C to 56.95 °C (average 44.59 °C), 41.84 °C to 50.74 °C (average 46.81 °C), and 45.67 °C to 60.75 °C (average 54.92 °C). In the stratigraphic profile (Fig. 12), temperature displays two distinct fluctuation cycles characterized by rising and falling trends from base to top, generally remaining within a high-temperature regime.

Keith and Weber (1964) combined $\delta^{13}C_{VPDB}$ and $\delta^{18}O_{VPDB}$ values to develop the isotope coefficient (Z value). This coefficient serves as a paleosalinity indicator, enabling differentiation between marine ($Z > 120$) and freshwater ($Z < 120$) depositional environments. The Z value is calculated as follows:

$$Z = 2.048 \times (\delta^{13}C_{VPDB} + 50) + 0.498 \times (\delta^{18}O_{VPDB} + 50)$$

The Z values of the analyzed samples range from 123.78 to 130.81, with an average of 127.89 (Table 1, Fig. 11B). All the samples exhibited Z values exceeding 120, indicating deposition in a marine environment. The Z values for stromatolites, thrombolites, oncoids, and botryoidal dolomites range from 129.21 to 130.47 (average 129.71), 124.84 to 130.81 (average 128.03), 126.62 to 130.71 (average 128.24), and 123.78 to 127.30 (average 125.91). Within the stratigraphic profile (Fig. 12), the Z value shows two sequential cycles of decline followed by an increase from the bottom up, indicating two phases of decreasing and subsequently increasing paleosalinity. This variation is likely associated with sea-level fluctuations, suggesting that two significant marine transgression-regression cycles occurred during the deposition of the upper Ediacaran Dengying Formation.

Stromatolites exhibit moderate $\delta^{13}C_{VPDB}$ values and positive $\delta^{18}O_{VPDB}$ values (Fig. 7). They are formed in marine depositional environments with moderate temperatures and high salinity. The t values of dispersed, layered, and reticular thrombolites increase progressively, whereas the Z values progressively decrease (Fig. 11). The sedimentary environment gradually changed from open shallow marine environment to restricted deepwater environment (Fig. 7). The $\delta^{13}C_{VPDB}$ and $\delta^{18}O_{VPDB}$ values of oncoids are moderate within the microbial dolomite (Fig. 7). They typically form in deepwater or more restricted environments. The Z values are slightly lower than those of stromatolites but still suggest a high-salinity marine depositional environment (Fig. 11). Botryoidal dolomites exhibit positive $\delta^{13}C_{VPDB}$ values and negative $\delta^{18}O_{VPDB}$ values (Fig. 7). The highest t value and the lowest Z value indicate high temperature depositional environment influenced by atmospheric freshwater (Fig. 11).

Sr/Ba ratio is commonly used to identify marine depositional environments (Epstein and Mayeda, 1953). Sr/Ba ratios greater than 1 are generally interpreted to indicate a saline environment; values between 0.6 and 1 suggest transitional settings, while values below 0.6 indicate freshwater conditions (Rimmer, 2004). All analyzed samples exhibit Sr/Ba ratios greater than 1 (Table 2). The environment remained a consistently saline marine environment. The botryoidal dolomites exhibit the lowest Sr/Ba ratios. Atmospheric precipitation leaching may have influenced their formation, potentially contributing to a slight reduction in salinity. Stratigraphically, the Sr/Ba ratios exhibit two sequential cycles of decrease followed by increase (Fig. 12). The ancient seawater salinity experienced two cycles of decrease and increase.

Redox conditions influence the geochemical characteristics, causing

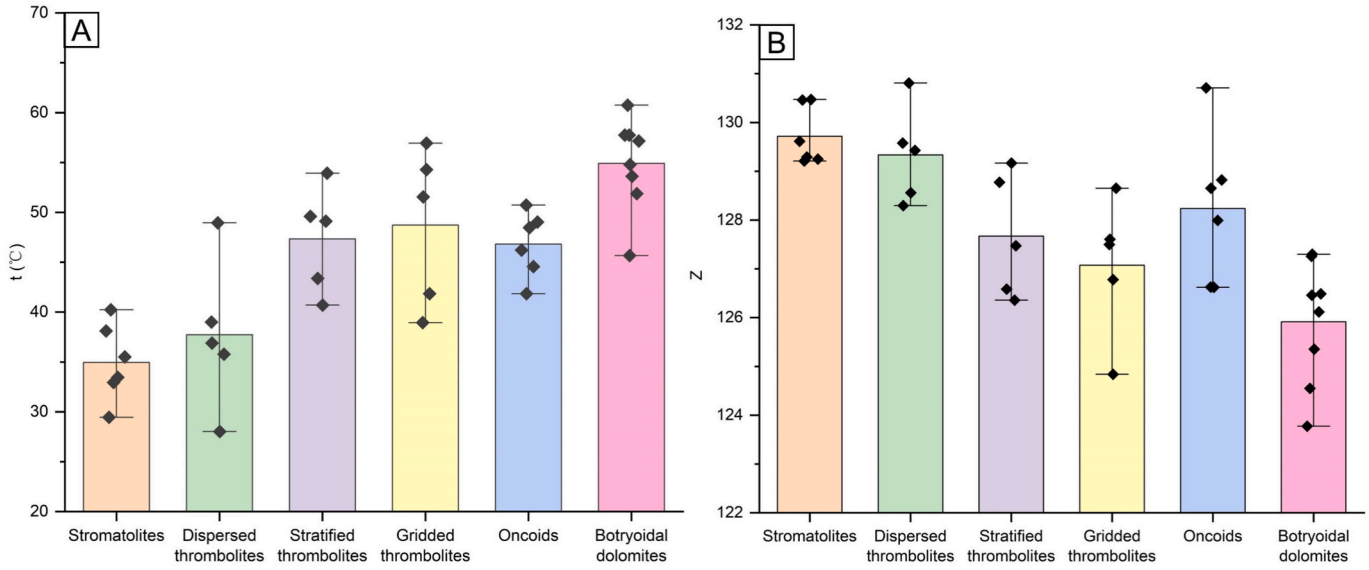

Fig. 11. *t* and Z values of microbial dolomites.

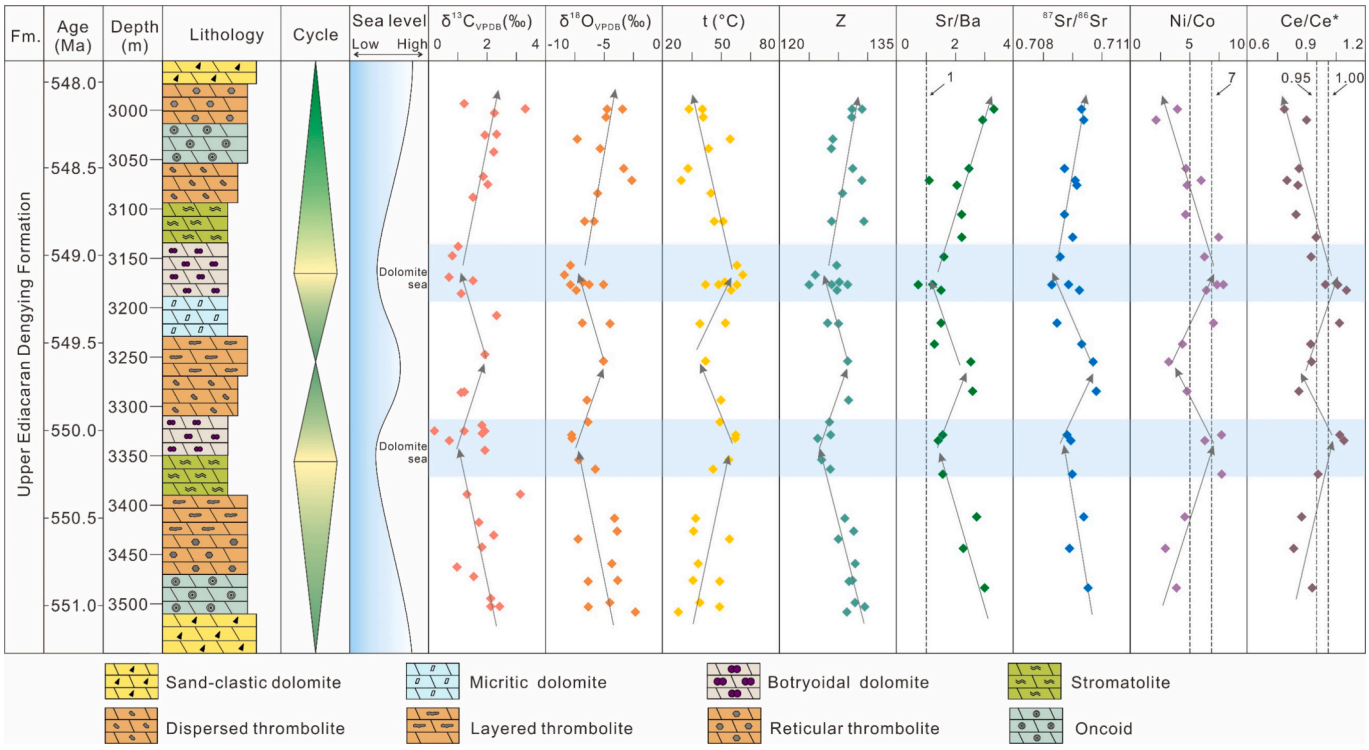

Fig. 12. The vertical distribution of sedimentary lithology and geochemical elements cycles. In the vertical direction, two transgression and regression cycles can be identified. Two stages of the dolomite sea are developed, which are characterized by high temperature, low salinity, and anoxic reduction conditions.

sediments under different redox conditions to exhibit distinct element signatures (Bi et al., 2021). The Ni/Co ratio serves as a widely accepted redox proxy: values below 5 indicate oxidizing conditions, 5–7 correspond to suboxic conditions, and values above 7 suggest anoxic environments (Jones and Manning, 1994). Most samples exhibit Ni/Co ratios below 7 (Table 2). The environment was predominantly characterized by oxidizing to suboxic conditions. The botryoidal dolomites recorded the highest Ni/Co ratio, with an average value of 7.048. They were deposited under suboxic to anoxic conditions. Vertically, Ni/Co ratios increase and decrease twice from bottom to top (Fig. 12). The redox environment experienced shifts between oxidizing and anoxic conditions in two cycles.

The Ce anomaly serves as an indicator of the redox conditions of ancient seawater (Moffett, 1990). Ce/Ce* values below 0.95 represent a negative Ce anomaly and are suggestive of oxidizing seawater conditions. Ce/Ce* values exceeding 1 indicate a positive Ce anomaly, reflecting a transition to weakly oxidizing or anoxic environments (Bau and Dulski, 1996; Wu et al., 2019). The Ce anomaly values in the samples range from 0.789 to 1.104 (Fig. 8B). Most samples show a negative Ce anomaly, indicating that the environment was predominantly oxidizing. However, compared to the Ce/Ce* values in modern seawater (ranging from 0.1 to 0.6), the magnitude of the negative Ce anomaly is

less pronounced. While oxygenation had begun, oxygen levels had not yet reached typical Phanerozoic concentrations. Stratigraphically, Ce anomalies exhibit two cycles of increase and decrease, reflecting two redox transitions between oxidizing and anoxic conditions (Fig. 12).

Eu typically exists as Eu^{3+} under standard conditions. Under reducing conditions, part of Eu^{3+} is reduced to Eu^{2+} (Michard et al., 1983). In high-temperature conditions, Eu^{3+} is more readily converted to the less soluble Eu^{4+}, which results in Eu enrichment and manifests as a positive anomaly (Frei et al., 2017). A Eu/Eu* value greater than 1 is referred to as a positive Eu anomaly, while a value less than 1 indicates a negative anomaly (Lawrence et al., 2006). In the study area, Eu primarily exhibits a positive anomaly (Fig. 8B). The upper Ediacaran Dengying Formation experienced high-temperature conditions, consistent with the previously discussed temperature indicators.

Carbonate minerals precipitated from different fluid environments exhibit distinct REY distribution patterns (Bi et al., 2021). These patterns serve as effective indicators for tracing the sources of fluids responsible for carbonate deposition and diagenesis (Michard et al., 1983). Different types of microbial dolomite display similar REY enrichment patterns (Fig. 8F). They were formed in similar seawater chemical environments. The shale-normalized REY distribution patterns of modern seawater are characterized by HREE enrichment, coupled with positive La anomalies, negative Ce anomalies, and weakly positive Gd anomalies (Hatje et al., 2016; Oka et al., 2021). These geochemical signatures demonstrate similarities to those identified in the Ediacaran microbial dolomites analyzed in this study. The REY enrichment pattern ranges from flat to moderate. The LREY segment shows a leftward tilt, while the HREY segment exhibits a slight rightward tilt. The LREY/HREY ratio generally exceeds 0.5 (Fig. 8E). The samples are slightly deficient in LREY and enriched in HREY. This is consistent with the enrichment levels of LREY and HREY in typical seawater. Variations in the $(Nd/Yb)_n$ ratio are indicative of the relative enrichment of light versus heavy REY (Riaz et al., 2020). In most samples, $(Nd/Yb)_n$ ratios are less than 1 (Fig. 8E). The differentiation of REY is relatively low overall. The microbial dolomites were primarily formed by direct seawater precipitation and underwent limited diagenesis. REY redistribution and migration were minimal, leading to a low degree of elemental differentiation.

5.3. *Paleoenvironmental evolution of upper Ediacaran Dengying Formation (ca 551.1 to 542.0 Ma)*

During the Neoproterozoic glaciation, intense continental weathering occurred under specific tectonic conditions (Dong et al., 2006). This process, combined with global icehouse climates and anoxic ferruginous oceans, dramatically altered Mg cycling. Enhanced Mg input from the continent, coupled with reduced extraction from the ocean, resulted in extremely high oceanic Mg/Ca ratios (Hood et al., 2022). At the end of the Ediacaran, in the Upper Yangtze region, the environment was primarily dominated by an aragonite sea (with Mg/Ca ratios > 2), and the regional development of a transient "dolomite sea" (with Mg/Ca ratios > 10) (Shuster et al., 2018). Previous studies have demonstrated that primary dolomite precipitation can occur under specific conditions (Daye et al., 2019; Roberts et al., 2013; Vasconcelos et al., 1995). The experimental conditions included high Mg/Ca ratios, organic-rich environments (high carboxyl concentrations), high salinity, and certain concentrations of Mn^{2+}, among other factors. These conditions closely align with the characteristics of Neoproterozoic seawater (Wood et al., 2018). The increase in oceanic Mg/Ca ratios and alkalinity during the glacial period likely facilitated dolomite precipitation (Han et al., 2022). These factors are linked to the increased continental weathering flux following the Sturtian glaciation event (Williams et al., 2019). Dolomite precipitation may have also been influenced by the low sulfate levels in Neoproterozoic oceans. Lower sulfate concentrations reduce the metabolic activity of sulfate-reducing bacteria, facilitating the binding of Mg with Ca to form dolomite (Chang et al., 2020). The "Snowball Earth" event concluded at the end of the Cryogenian. Global warming, glacier melt, and crustal uplift caused by plate rifting resulted in significant increases in both global and regional sea levels (Fang, 2022). The Ediacaran period entered into a stable, warm phase, accompanied by notable variations in sea level and salinity. Periodic oxidation events accompanied this, and atmospheric oxygen concentrations gradually increased (Hood et al., 2022; Li et al., 2023b). The surface ocean was dominated by oxygenated seawater, whereas the deeper ocean primarily contained anoxic water (Thomas and Catling, 2024).

The microbial dolomites of the upper Ediacaran Dengying Formation offer valuable insights into the dynamic interactions between microbial communities, seawater chemistry, and environmental change during a pivotal interval in Earth's history. The observed dolomite structures reflect microbial adaptation to variable redox and salinity conditions across a shallow restricted platform setting. These features suggest that microbial ecosystems were able to thrive in low-oxygen, high-salinity, and low-sulfate conditions, which may have been widespread in Precambrian oceans. The depositional history of the Dengying Formation appears to have been episodic, with intermittent subaerial exposure (Cui et al., 2019). The residence time of Sr in seawater exceeds 1 Myr, while its mixing time in seawater is only 1 Kyr (Palmer and Elderfield, 1985). Consequently, the $^{87}Sr/^{86}Sr$ ratio of seawater remains globally uniform within a given geological period (Alexander Bentley, 2006). The $^{87}Sr/^{86}Sr$ ratio can serve as an indicator of sea level changes (Blum and Erel, 1995). The $^{87}Sr/^{86}Sr$ ratio and sea-level changes are inversely correlated (Zhang et al., 2022b). The stratigraphic profile reveals two cycles of increasing and decreasing $^{87}Sr/^{86}Sr$ values (Table 2, Fig. 12). This suggests that two episodes of sea-level regression and transgression occurred during deposition.

During the early stage of deposition, no significant tectonic influence was observed (Zhang et al., 2024). Sea level changes were likely controlled by climatic and other environmental factors (Chang et al., 2020). During this time, sea levels were high, the climate was warm, salinity was elevated, and oxidizing conditions prevailed (Lan et al., 2022). This environment primarily favored the formation of microbial dolomites such as stromatolites, thrombolites, and oncoids. Enhanced evaporation under warm conditions likely contributed to a subsequent sea-level fall, leading to the exposure of shallow marine areas and the intensification of local evaporation (Wang et al., 2020). This process promoted dissolution, resulting in the formation of fractures and cavities. Reduced water circulation limited oxygen replenishment, creating low-oxygen or anoxic conditions (Wood et al., 2018). These conditions may have led to the development of the first phase of a regional "dolomite sea". Following a transgression, these cavities were filled with seawater, leading to the formation of botryoidal dolomites.

Subsequently, under the influence of global climate change, the rise in sea level caused by glacial melting led to the inland transgression of seawater (Li et al., 2024). The increase in water depth has submerged areas that were previously above sea level. The previously isolated inland seas were reconnected to the open ocean, leading to higher salinity. Enhanced hydrodynamic exchange associated with increased depth improved water circulation, contributing to a gradual rise in oxygenation. Although temperatures slightly decreased, the environment remained generally warm overall. The resulting redistribution of water depth, temperature, and salinity facilitated alternating oxic and anoxic conditions, which were favorable for the deposition of microbial dolomites, including stromatolites, thrombolites, and oncoids.

At the end of deposition, tectonic uplift related to the Tongwan Movement I induced a relative sea-level fall across the Yangtze Platform, exposing its margins to subaerial erosion (Wang et al., 2014). The uplift likely enhanced hydrodynamic conditions, increasing the transport, redeposition, and erosion of the platform edge sediments. With sea-level regression, salinity may have decreased slightly due to freshwater influx or atmospheric precipitation, and reduced circulation led to lower oxygen concentrations, fostering an anoxic environment (Ding et al., 2021). During this period, the Sichuan Basin was positioned in a low-

latitude equatorial setting (Li et al., 2013). The persistently high temperatures sustained elevated seawater temperatures and favored microbial activity and carbonate production. A second phase of the "dolomite sea" may have formed under these conditions. Fractures and cavities were periodically filled with seawater during sea-level fluctuations, facilitating the formation of a large-scale botryoidal dolomite deposit (Wang et al., 2020). Following the Tongwan Movement I, a subsequent sea-level rise restored shallow marine environments, characterized by increased salinity, elevated oxygen levels, and enhanced microbial productivity, which once again governed sedimentary processes (Ding et al., 2021).

The microbial dolomites of the upper Ediacaran Dengying Formation not only hold significant implications for hydrocarbon reservoir development in South China, but also serve as a model archive for reconstructing microbial behavior, carbonate factory evolution, and paleoclimate dynamics in Earth's geologic and biologic history. Similar microbial dolomite reservoirs have been documented in other late Ediacaran to early Cambrian successions worldwide, such as the Nama Group in Namibia, the Wonoka Formation in South Australia, and the Ara Group in Oman (Amthor et al., 2003; Schröder et al., 2005; Williams and Schmidt, 2018; Wood et al., 2023). The widespread distribution of such microbial dolomites underscores the global microbial ecosystems capable of influencing carbonate diagenesis and reservoir quality.

Moreover, the geochemical signatures preserved within these microbial dolomites reflect major paleoenvironmental shifts following the Marinoan glaciation. Post-glacial greenhouse conditions likely stimulated elevated microbial activity, influencing carbonate saturation states and promoting dolomite precipitation under low-oxygen, high-salinity conditions (Fang, 2022; Hood et al., 2022; Li et al., 2023b). Associated variations in seawater chemistry, such as fluctuations in Sr isotopes, REY patterns, and redox-sensitive trace elements can be linked to continental weathering and hydrothermal fluxes driven by sea-level oscillations and intensified plate tectonics (Meyer et al., 2012; Wang et al., 2023; Zhang et al., 2022b). These findings highlight the complex interplay among microbial processes, climate variability, and tectonic evolution in shaping Precambrian carbonate reservoirs. Furthermore, they establish the Dengying Formation as a reference system for studying early Earth environments and their resource potential.

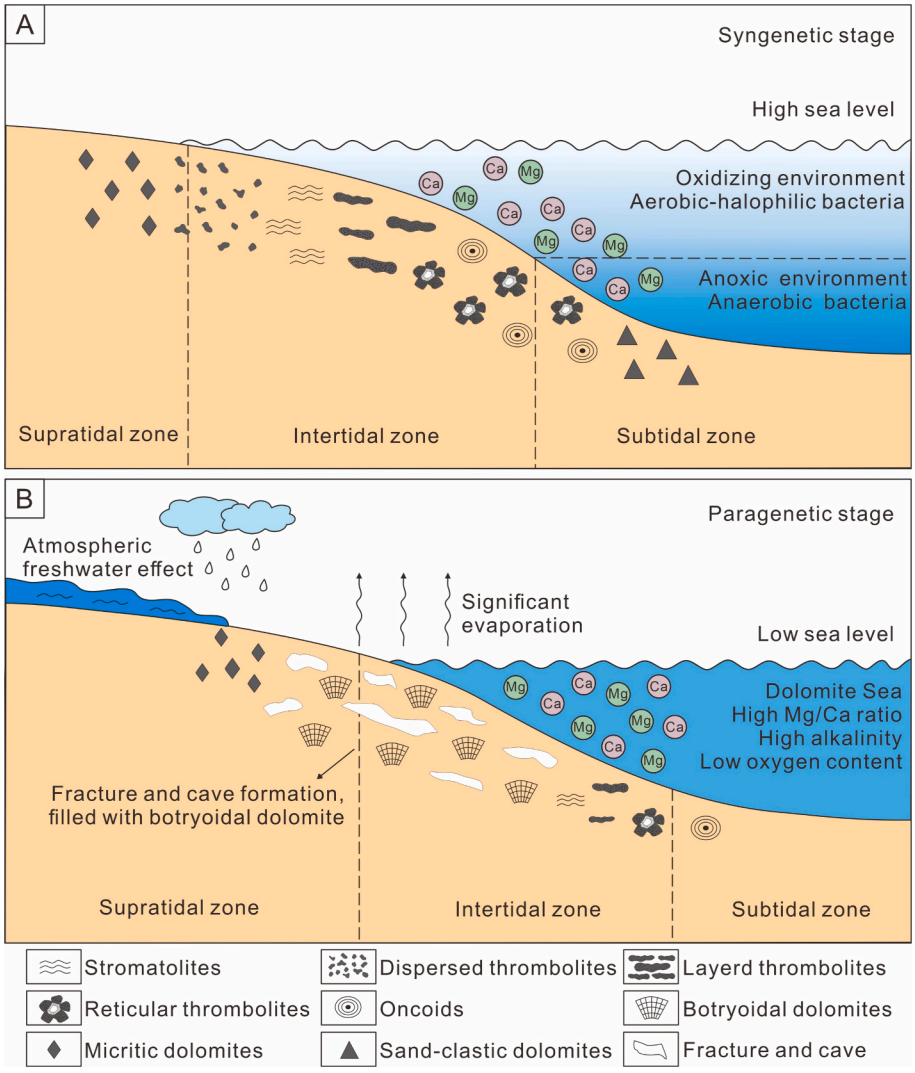

Fig. 13. Sedimentary model of the upper Ediacaran Dengying Formation microbial dolomites. (A) Syngenetic stage model. During this stage, sea level and salinity are elevated, the climate is warm, and oxygen content is high. Microbial dolomite formation is primarily facilitated by aerobic-halophilic bacteria in the supratidal zone and anaerobic bacteria in the subtidal zone. (B) Penecontemporaneous stage model. During this period, a "dolomite sea" developed. As sea level decreases, evaporation intensifies, and oxygen content diminishes. The surface undergoes dissolution by atmospheric freshwater, creating voids that are subsequently filled with seawater, resulting in botryoidal dolomite.

5.4. Sedimentary model of the upper Ediacaran Dengying Formation microbial dolomites

The syngenetic stage is typically associated with rising sea levels (Fig. 13A). The widespread intrusion of seawater leads to the formation of extensive shallow marine environments. During this period, enhanced water movement and exchange facilitate the dissolution and distribution of oxygen, thereby creating an oxidizing environment. During the deposition of the Dengying Formation, the Sichuan Basin was situated near the equator, where the climate was warm (Li et al., 2013). Elevated temperatures led to increased evaporation, which in turn raised seawater salinity. Higher salinity is conducive to microbially induced dolomite precipitation (Qiu et al., 2017). In intertidal and supratidal zones, water is shallow and oxygen levels are elevated. Dolomites are primarily precipitated through the metabolic activity of aerobic-halophilic bacteria, such as cyanobacteria (Thompson and Ferris, 1990). This process may occur not only during microbial metabolism but also post-mortem, as the degradation of EPS continues to influence sediment calcification (Reid et al., 2024).

Microbial communities commonly develop abundant negatively charged surface functional groups (e.g., carboxyl, phosphoryl, hydroxyl). These groups selectively concentrate inorganic ions like Ca^{2+} and Mg^{2+}, ultimately establishing localized supersaturation conditions required for dolomite crystallization (Liu et al., 2024). Moreover, microbial EPS and associated functional groups are capable of reducing the hydration energy barrier of Mg^{2+}, thereby enhancing dolomite nucleation (Del Buey et al., 2021). Microbial metabolism also plays a crucial role in modifying water chemistry, fostering microenvironments that promote dolomite precipitation (Jiang et al., 2021). Below the subtidal zone, anoxic redox environments dominate. Dolomite precipitation is primarily promoted by the activity of anaerobic bacteria, such as sulfate-reducing bacteria and methanogens (Liu et al., 2020). These microbes consume organic matter, reduce sulfate concentrations, and release CO_3^{2-} and Mg^{2+}, increasing alkalinity and thus facilitating dolomite precipitation (Ma et al., 2020). Concurrently, pyrite (FeS_2) and magnetite (FeS) are formed.

During the penecontemporaneous stage (Fig. 13B), as sea levels declined, intensified evaporation of local water occurred. Exposed platforms and shallow marine zones experienced significant evaporation, reducing water flow and decreasing dissolved oxygen levels in seawater. This led to the development of low-oxygen or anoxic environments. Reduced oxygen levels may enhance microbial dolomite formation by stimulating the activity of anaerobic microorganisms, such as sulfate-reducing bacteria (Jiang et al., 2024). The sea-level fall also caused exposure of the upper Ediacaran Dengying Formation to meteoric freshwater, which dissolved carbonate minerals and produced fractures and cavities. Subsequent sea-level rise permitted seawater infiltration into these voids, which resulted in the precipitation of fibrous dolomite both above preexisting microbial dolomites and within the newly formed pores. Fibrous dolomite cement is typically associated with the seawater seepage zone, although some may also form in the seawater infiltration zone. Additionally, granular isopachous rims are characteristics of the freshwater seepage zone (Hu et al., 2020).

The depositional and geochemical characteristics of the upper Ediacaran Dengying Formation can be better contextualized through comparison with coeval carbonate successions worldwide. For instance, the Nama Group exhibits a similar development of thrombolitic microbialites and pervasive early dolomitization, indicative of microbial mediation in low-sulfate, shallow-marine settings (Wood et al., 2023). The Ara Group records evaporitic sabkha-like conditions with abundant botryoidal and spheroidal dolomites, which have also been interpreted as products of microbial processes under restricted marine conditions (Amthor et al., 2003). The Wonoka Formation preserves globally geochemical signatures, such as Precambrian negative $\delta^{13}C_{VPDB}$ excursion and concomitant decline in $^{87}Sr/^{86}Sr$ ratios, which closely mirror the isotopic stratigraphy documented in the Dengying Formation (Williams and Schmidt, 2018). It becomes evident that the microbial dolomites of the Dengying Formation were part of a globally distributed carbonate factory active during the terminal Ediacaran. This highlights the importance of microbial mediation in carbonate systems during periods of major oceanic and biogeochemical transition, and places the Dengying Formation within the framework of global Ediacaran environmental evolution.

6. Conclusions

The microbial dolomites (stromatolites, thrombolites, oncoids, and botryoidal dolomites) in the upper Ediacaran Dengying Formation of the central Sichuan Basin reveal interactions between microbial communities and depositional environments within a shallow restricted platform. The conclusions are summarized as follows:

(1) The diversity of microbial dolomite structure is controlled by the interplay of hydrodynamic energy and microbial activity. Stromatolites and botryoidal dolomites are formed in low-energy settings with strong microbial activity, while dispersed thrombolites dominate under weak microbial influence. High-energy environments favored the development of layered and reticular thrombolites and oncoids through particle aggregation.
(2) Two transgressive–regressive cycles have been identified, driven by global climate fluctuations and regional tectonic activity (Tongwan Movement I). These cycles correspond to two “dolomite sea” events: the first is linked to evaporation and localized anoxia, and the second is controlled by tectonic uplift and sedimentary reworking, highlighting the critical role of regional tectonics in reservoir formation.
(3) Geochemical indicators record post-glacial oceanographic transitions, including seawater stratification and continental weathering changes, providing new constraints on the environmental context for the rise of complex life during the Ediacaran-Cambrian transition. Comparative studies with global analogues demonstrate the widespread microbial diagenetic processes during the Ediacaran and further emphasize the unique tectono-climatic cyclicity of the Sichuan Basin. Although diagenesis may partially obscure isotopic and REY signals, the systematic study of microbial dolomites in the Dengying Formation is particularly significant for the reconstruction of the late Precambrian earth system, especially for understanding Precambrian seawater chemistry, microbial evolution and early carbonate reservoir development.

7. Author statement

The authors affirm that this manuscript is an original work and has not been submitted or published elsewhere. All authors have significantly contributed to the conception, design, data analysis, and writing of this manuscript. All necessary approvals and consents have been obtained, and the manuscript has been approved by all co-authors for submission.

CRediT authorship contribution statement

Yuan Zhou: Conceptualization, Writing – original draft, Formal analysis, Project administration. **Xuelian You:** Visualization, Investigation, Data curation. **Qing Li:** Writing – review & editing, Project administration, Resources, Funding acquisition. **Zhuofeng Zhang:** Methodology, Visualization, Investigation. **Qiang Du:** Data curation, Supervision, Methodology. **Zhengyu Wei:** Validation, Methodology, Supervision. **Xinlong Li:** Investigation, Data curation. **Hui Zhou:** Resources, Supervision.

Declaration of competing interest

The authors declare that they have no known competing financial interests or personal relationships that could have appeared to influence the work reported in this paper.

Acknowledgements

This study was financially supported by the National Science and Technology Major Project (No. 2025ZD1406403-02), the National Natural Science Foundation of China (Grant No. 42372146 and 41972107). We are grateful to the Research Institute of Petroleum Exploration and Development, PetroChina for providing research funding, data access and for permission to publish.

Data availability

I have shared the link to my data at the Attach file step

References

Alexander Bentley, R., 2006. Strontium Isotopes from the Earth to the Archaeological Skeleton: a Review. J. Archaeol. Method Theory 13, 135–187. https://doi.org/10.1007/s10816-006-9009-x.

Al-Siyabi, H.A., 2005. Exploration history of the Ara intrasalt carbonate stringers in the South Oman Salt Basin. GeoArabia 10, 39–72. https://doi.org/10.2113/geoarabia100439.

Amthor, J.E., Grotzinger, J.P., Schröder, S., Bowring, S.A., Ramezani, J., Martin, M.W., Matter, A., 2003. Extinction of cloudina and namacalathus at the precambrian-cambrian boundary in Oman. Geology 31, 431. https://doi.org/10.1130/0091-7613(2003)031<0431:EOCANA>2.0.CO;2.

Awramik, S.M., 1971. Precambrian columnar stromatolite diversity: reflection of metazoan appearance. Science 174, 825–827. https://doi.org/10.1126/science.174.4011.825.

Bau, M., Dulski, P., 1996. Distribution of yttrium and rare-earth elements in the Penge and Kuruman iron-formations, Transvaal Supergroup, South Africa. Precambr. Res. 79, 37–55. https://doi.org/10.1016/0301-9268(95)00087-9.

Bernhard, J.M., Fisher, L.A., Murphy, Q., Sen, L., Yeh, H.D., Louyakis, A., Gomaa, F., Reilly, M., Batta-Lona, P.G., Bucklin, A., Le Roux, V., Visscher, P.T., 2023. Transition from stromatolite to thrombolite fabric: potential role for reticulopodial protists in lake microbialites of a Proterozoic ecosystem analog. Front. Microbiol. 14, 1210781. https://doi.org/10.3389/fmicb.2023.1210781.

Bi, D., Shi, X., Huang, M., Yu, M., Zhou, T., Zhang, Y., Zhu, A., Shi, M., Fang, X., 2021. Geochemical and mineralogical characteristics of deep-sea sediments from the western North Pacific Ocean: Constraints on the enrichment processes of rare earth elements. Ore Geol. Rev. 138, 104318. https://doi.org/10.1016/j.oregeorev.2021.104318.

Blum, J.D., Erel, Y., 1995. A silicate weathering mechanism linking increases in marine 87Sr/ 86Sr with global glaciation. Nature 373, 415–418. https://doi.org/10.1038/373415a0.

Bosak, T., Knoll, A.H., Petroff, A.P., 2013. The Meaning of Stromatolites. Annu. Rev. Earth Planet. Sci. 41, 21–44. https://doi.org/10.1146/annurev-earth-042711-105327.

Bowyer, F.T., Krause, A.J., Song, Y., Huang, K.-J., Fu, Y., Shen, B., Li, J., Zhu, X.-K., Kipp, M.A., Van Maldegem, L.M., Brocks, J.J., Shields, G.A., Le Hir, G., Mills, B.J.W., Poulton, S.W., 2023. Biological diversification linked to environmental stabilization following the Sturtian Snowball glaciation. Sci. Adv. 9, eadf9999. https://doi.org/10.1126/sciadv.adf9999.

Braissant, O., Cailleau, G., Dupraz, C., Verrecchia, E.P., 2003. Bacterially induced mineralization of calcium carbonate in terrestrial environments: the role of exopolysaccharides and amino acids. J. Sediment. Res. 73, 485–490. https://doi.org/10.1306/111302730485.

Burne, R.V., Moore, L.S., 1987. Microbialites: organosedimentary deposits of benthic microbial communities. PALAIOS 2, 241. https://doi.org/10.2307/3514674.

Centeno, C.M., Legendre, P., Beltrán, Y., Alcántara-Hernández, R.J., Lidström, U.E., Ashby, M.N., Falcón, L.I., 2012. Microbialite genetic diversity and composition relate to environmental variables. FEMS Microbiol. Ecol. 82, 724–735. https://doi.org/10.1111/j.1574-6941.2012.01447.x.

Chacón-Baca, E., Romero De La Cruz, O., Chavez-Cabello, G., Cienfuegos Alvarado, E., Morales-Puente, P., Alba-Aldave, L., Blanco Lanza, S., 2024. The generation of a clotted peloidal micrite fabric by endolithic cyanobacteria in recent thrombolites from Cuatro Cienegas, northern Mexico. Sedimentology 71, 2290–2313. https://doi.org/10.1111/sed.13215.

Chang, B., Li, C., Liu, D., Foster, I., Tripati, A., Lloyd, M.K., Maradiaga, I., Luo, G., An, Z., She, Z., Xie, S., Tong, J., Huang, J., Algeo, T.J., Lyons, T.W., Immenhauser, A., 2020. Massive formation of early diagenetic dolomite in the Ediacaran ocean: constraints on the "dolomite problem. PNAS 117, 14005–14014. https://doi.org/10.1073/pnas.1916673117.

Condon, D., Zhu, M., Bowring, S., Wang, W., Yang, A., Jin, Y., 2005. U-Pb ages from the neoproterozoic Doushantuo Formation, China. science 308 (5718), 95–98.

Cui, H., Kaufman, A.J., Xiao, S., Zhou, C., Liu, X.-M., 2017. Was the Ediacaran Shuram Excursion a globally synchronized early diagenetic event? Insights from methane-derived authigenic carbonates in the uppermost Doushantuo Formation, South China. Chem. Geol. 450, 59–80. https://doi.org/10.1016/j.chemgeo.2016.12.010.

Cui, H., Xiao, S., Cai, Y., Peek, S., Plummer, R.E., Kaufman, A.J., 2019. Sedimentology and chemostratigraphy of the terminal Ediacaran Dengying Formation at the Gaojiashan section, South China. Geol. Mag. 156, 1924–1948. https://doi.org/10.1017/S0016756819000293.

Dahanayake, K., 1978. Sequential position and environmental significance of different types of oncoids. Sed. Geol. 20, 301–316. https://doi.org/10.1016/0037-0738(78)90060-X.

Daye, M., Higgins, J., Bosak, T., 2019. Formation of ordered dolomite in anaerobic photosynthetic biofilms. Geology 47, 509–512. https://doi.org/10.1130/G45821.1.

Del Buey, P., Sanz-Montero, M.E., Braissant, O., Cabestrero, Ó., Visscher, P.T., 2021. The role of microbial extracellular polymeric substances on formation of sulfate minerals and fibrous Mg-clays. Chem. Geol. 581, 120403. https://doi.org/10.1016/j.chemgeo.2021.120403.

Diaz, M.R., Eberli, G.P., Blackwelder, P., Phillips, B., Swart, P.K., 2017. Microbially mediated organomineralization in the formation of ooids. Geology 45, 771–774. https://doi.org/10.1130/G39159.1.

Ding, Y., Li, Z., Liu, S., Song, J., Zhou, X., Sun, W., Zhang, X., Li, S., Ran, B., Peng, H., Li, Z., Wang, H., Chen, D., 2021. Sequence stratigraphy and tectono-depositional evolution of a late Ediacaran epeiric platform in the upper Yangtze area South China. Precambrian Research 354, 106077. https://doi.org/10.1016/j.precamres.2020.106077.

Dong, F., Chen, Liu, 2006. Formation of late neoproterozoic cap carbonates and termination mechanism of "Snowball Earth". Acta Sedimentol. Sin. https://doi.org/10.1007/s11442-006-0415-5.

Dupraz, C., Reid, R.P., Braissant, O., Decho, A.W., Norman, R.S., Visscher, P.T., 2009. Processes of carbonate precipitation in modern microbial mats. Earth Sci. Rev. 96, 141–162. https://doi.org/10.1016/j.earscirev.2008.10.005.

Dupraz, C., Visscher, P.T., 2005. Microbial lithification in marine stromatolites and hypersaline mats. Trends Microbiol. 13, 429–438. https://doi.org/10.1016/j.tim.2005.07.008.

Ehrlich, H., 1998. Geomicrobiology: its significance for geology. Earth Sci. Rev. 45, 45–60. https://doi.org/10.1016/S0012-8252(98)00034-8.

Emrich, K., Ehhalt, D.H., Vogel, J.C., 1970. Carbon isotope fractionation during the precipitation of calcium carbonate. Earth Planet. Sci. Lett. 8, 363–371. https://doi.org/10.1016/0012-821X(70)90109-3.

Epstein, S., Mayeda, T., 1953. Variation of O18 content of waters from natural sources. Geochim. Cosmochim. Acta 4, 213–224. https://doi.org/10.1016/0016-7037(53)90051-9.

Fang, Y., 2022. Coupled dolomite and silica precipitation from continental weathering during deglaciation of the Marinoan Snowball Earth. Precambr. Res. 380, 106824. https://doi.org/10.1016/j.precamres.2022.106824.

Fischer, W.W., Knoll, A.H., 2006. An iron shuttle for deepwater silica in late Archean and early Paleoproterozoic iron formation. Geol. Soc. Am. Bull. Preprint 1. https://doi.org/10.1130/B26328.1.

Frei, R., Døssing, L.N., Gaucher, C., Boggiani, P.C., Frei, K.M., Bech Árting, T., Crowe, S. A., Freitas, B.T., 2017. Extensive oxidative weathering in the aftermath of a late Neoproterozoic glaciation – evidence from trace element and chromium isotope records in the Urucum district (Jacadigo Group) and Puga iron formations (Mato Grosso do Sul, Brazil). Gondw. Res. 49, 1–20. https://doi.org/10.1016/j.gr.2017.05.003.

Galili, N., Shemesh, A., Yam, R., Brailovsky, I., Sela-Adler, M., Schuster, E.M., Collom, C., Bekker, A., Planavsky, N., Macdonald, F.A., Préat, A., Rudmin, M., Trela, W., Sturesson, U., Heikoop, J.M., Aurell, M., Ramajo, J., Halevy, I., 2019. The geologic history of seawater oxygen isotopes from marine iron oxides. Science 365, 469–473. https://doi.org/10.1126/science.aaw9247.

Gradstein, F.M., Ogg, J.G., Smith, A.G., Bleeker, W., Lourens, L.J., 2004. A new Geologic Time Scale, with special reference to Precambrian and Neogene. Episodes 27, 83–100. https://doi.org/10.18814/epiiugs/2004/v27i2/002.

Han, Z., Qi, P., Zhao, Y., Guo, N., Yan, H., Tucker, M.E., Li, D., Wang, J., Zhao, H., 2022. High Mg/Ca molar ratios promote protodolomite precipitation induced by the extreme halophilic bacterium vibrio harveyi QPL2. Front. Microbiol. 13, 821968. https://doi.org/10.3389/fmicb.2022.821968.

Hartley, A.M., House, W.A., Leadbeater, B.S.C., Callow, M.E., 1996. The use of microelectrodes to study the precipitation of calcite upon algal biofilms. J. Colloid Interface Sci. 183, 498–505. https://doi.org/10.1006/jcis.1996.0573.

Hatje, V., Bruland, K.W., Flegal, A.R., 2016. Increases in anthropogenic gadolinium anomalies and rare earth element concentrations in san francisco bay over a 20 year record. Environ. Sci. Technol. 50, 4159–4168. https://doi.org/10.1021/acs.est.5b04322.

He, D., Ma, Y., Li, Y., Wu, S., 2019. New directions in an established gas play: promising dolomite reservoirs in the Middle Triassic Leikoupo Formation of the Sichuan Basin China. Bulletin 103, 1–29. https://doi.org/10.1306/05111816502.

Hood, A.S., Penman, D.E., Lechte, M.A., Wallace, M.W., Giddings, J.A., Planavsky, N.J., 2022. Neoproterozoic syn-glacial carbonate precipitation and implications for a snowball Earth. Geobiology 20, 175–193. https://doi.org/10.1111/gbi.12470.

Hu, A., 2019. Dolomite genesis and reservoir-cap rock assemblage in carbonate-evaporite paragenesis system. Pet. Explor. Dev. 46, 969–982. https://doi.org/10.1016/S1876-3804(19)60253-3.

Hu, Y., Cai, C., Liu, D., Pederson, C.L., Jiang, L., Shen, A., Immenhauser, A., 2020. Formation, diagenesis and palaeoenvironmental significance of upper Ediacaran fibrous dolomite cements. Sedimentology 67, 1161–1187. https://doi.org/10.1111/sed.12683.

Jiang, W., Luo, Q., Shi, K., Liu, B., Wang, Y., Gao, X., 2021. Origin of a microbial-dominated carbonate reservoir in the lower Cambrian Xiaoerbulake Formation, Bachu-Tazhong area, Tarim Basin NW China. Mar. Petrol. Geol. 133, 105254. https://doi.org/10.1016/j.marpetgeo.2021.105254.

Jiang, Y., Gao, X., Yang, X., Gong, P., Pan, Z., Yi, L., Ma, S., Li, C., Kong, S., Wang, Y., 2024. Sulfate-reducing bacteria (SRB) mediated carbonate dissolution and arsenic release: Behavior and mechanisms. Sci. Total Environ. 929, 172572. https://doi.org/10.1016/j.scitotenv.2024.172572.

Jones, B., Manning, D.A.C., 1994. Comparison of geochemical indices used for the interpretation of palaeoredox conditions in ancient mudstones. Chem. Geol. 111, 111–129. https://doi.org/10.1016/0009-2541(94)90085-X.

Keith, M.L., Weber, J.N., 1964. Carbon and oxygen isotopic composition of selected limestones and fossils. Geochim. Cosmochim. Acta 28, 1787–1816. https://doi.org/10.1016/0016-7037(64)90022-5.

Knauth, L.P., 2005. Temperature and salinity history of the Precambrian ocean: implications for the course of microbial evolution. Palaeogeogr. Palaeoclimatol. Palaeoecol. 219, 53–69. https://doi.org/10.1016/j.palaeo.2004.10.014.

Lan, C., Xu, Z., Yang, D., Yang, W., Lu, C., Chen, H., Li, P., Wang, Y., Zou, H., 2022. Stratigraphy and depositional evolution of the terminal Ediacaran platform in the central to northern Sichuan Basin, Southwest China. Palaeogeogr. Palaeoclimatol. Palaeoecol. 601, 111142. https://doi.org/10.1016/j.palaeo.2022.111142.

Lawrence, M.G., Greig, A., Collerson, K.D., Kamber, B.S., 2006. Rare earth element and yttrium variability in South East Queensland waterways. Aquat. Geochem. 12, 39–72. https://doi.org/10.1007/s10498-005-4471-8.

Lee, J., Riding, R., 2023. Stromatolite-rimmed thrombolite columns and domes constructed by microstromatolites, calcimicrobes and sponges in late Cambrian biostromes, Texas. Sedimentology 70, 293–334. https://doi.org/10.1111/sed.13048.

Li, F., Deng, J., Kershaw, S., Burne, R., Gong, Q., Tang, H., Lu, C., Qu, H., Zheng, B., Luo, S., Jin, Z., Tan, X., 2021. Microbialite development through the Ediacaran–Cambrian transition in China: distribution, characteristics, and paleoceanographic implications. Global Planet. Change 205, 103586. https://doi.org/10.1016/j.gloplacha.2021.103586.

Li, M., Xu, Y., Sun, L., Chen, J., Zhang, K., Li, D., Farquhar, J., Zhang, X., Sun, R., Macdonald, F.A., Grasby, S.E., Fu, Y., Shen, Y., 2023a. Deglacial volcanism and reoxygenation in the aftermath of the Sturtian Snowball Earth. Sci. Adv. 9, eadh9502. https://doi.org/10.1126/sciadv.adh9502.

Li, T., Yang, W., Lu, C., Li, P., Xu, Z., He, Y., Duan, J., Zou, H., 2023b. Depositional processes of the mixed siliciclastic-carbonate system in the lower Cambrian Xiannüdong Formation in the northern Sichuan Basin South China. Mar. Petrol. Geol. 150, 106158. https://doi.org/10.1016/j.marpetgeo.2023.106158.

Li, W., Liu, J., Deng, S., Zhang, B., Zhou, H., 2015. The nature and role of Late Sinian-Early Cambrian tectonic movement in Sichuan Basin and its adjacent areas. Acta Petrolei Sinica 36, 546. https://doi.org/10.7623/syxb201505003.

Li, W., Yu, H., Deng, H., 2012. Stratigraphic division and correlation and sedimentary characteristics of the Cambrian in central-southern Sichuan Basin. Pet. Explor. Dev. 39, 725–735. https://doi.org/10.1016/S1876-3804(12)60097-4.

Li, X., Zhu, G., Zhang, Z., 2024. Genesis of ultra-deep dolostone and controlling factors of large-scale reservoir: a case study of the Sinian Dengying Formation and the Cambrian Longwangmiao Formation in the Sichuan Basin. Sci. China Earth Sci. 67, 2352–2382. https://doi.org/10.1007/s11430-023-1301-x.

Li, Z.X., 2003. Geochronology of Neoproterozoic syn-rift magmatism in the Yangtze Craton, South China and correlations with other continents: evidence for a mantle superplume that broke up Rodinia. Precambr. Res. 122, 85–109. https://doi.org/10.1016/S0301-9268(02)00208-5.

Li, Z.-X., Evans, D.A.D., Halverson, G.P., 2013. Neoproterozoic glaciations in a revised global palaeogeography from the breakup of Rodinia to the assembly of Gondwanaland. Sed. Geol. 294, 219–232. https://doi.org/10.1016/j.sedgeo.2013.05.016.

Lin, X., Peng, J., Du, L., Yan, J., Hou, Z., 2017. Characterization of the Microbial Dolomite of the Upper Sinian Dengying Formation in the Hanyuan Area of Sichuan Province, China. Acta Geologica Sinica - English Edition 91, 806–821. https://doi.org/10.1111/1755-6724.13311.

Ling, H.-F., Chen, X., Li, D., Wang, D., Shields-Zhou, G.A., Zhu, M., 2013. Cerium anomaly variations in Ediacaran–earliest Cambrian carbonates from the Yangtze Gorges area, South China: Implications for oxygenation of coeval shallow seawater. Precambr. Res. 225, 110–127. https://doi.org/10.1016/j.precamres.2011.10.011.

Liu, C., Wang, Z., Raub, T.D., Macdonald, F.A., Evans, D.A.D., 2014. Neoproterozoic cap-dolostone deposition in stratified glacial meltwater plume. Earth Planet. Sci. Lett. 404, 22–32. https://doi.org/10.1016/j.epsl.2014.06.039.

Liu, D., Chen, T., Dai, Z., Papineau, D., Qiu, X., Wang, H., Benzerara, K., 2024. A non-classical crystallization mechanism of microbially-induced disordered dolomite. Geochim. Cosmochim. Acta 381, 198–209. https://doi.org/10.1016/j.gca.2024.05.005.

Liu, D., Fan, Q., Papineau, D., Yu, N., Chu, Y., Wang, H., Qiu, X., Wang, X., 2020. Precipitation of protodolomite facilitated by sulfate-reducing bacteria: the role of capsule extracellular polymeric substances. Chem. Geol. 533, 119415. https://doi.org/10.1016/j.chemgeo.2019.119415.

Liu, S., Yang, Y., Deng, B., Zhong, Y., Wen, L., Sun, W., Li, Z., Jansa, L., Li, J., Song, J., Zhang, X., Peng, H., 2021. Tectonic evolution of the Sichuan Basin Southwest China. Earth-Science Reviews 213, 103470. https://doi.org/10.1016/j.earscirev.2020.103470.

Liu, S.G., Sun, W., Luo, Z.L., Song, J.M., Peng, H.L., 2013. Xingkai taphrogenesis and petroleum exploration from Upper Sinian to Cambrian Strata in Sichuan Basin, China. Journal of Chengdu University of Technology (Science and Technology Edition) 40, 511–520. https://doi.org/10.3969/j.issn.1671-9727.2013.05.03.

Ma, B., Cao, Y., Eriksson, K.A., 2020. Microbially induced dolomite precipitates in Eocene lacustrine siliciclastic sequences in the Dongying depression, Bohai Bay Basin, China: Evidence from petrology, geochemistry, and numerical modeling. AAPG Bulletin 104, 2051–2075. https://doi.org/10.1306/10191918225.

Manche, C.J., Kaczmarek, S.E., 2019. Evaluating reflux dolomitization using a novel high-resolution record of dolomite stoichiometry: a case study from the cretaceous of central Texas, USA. Geology 47, 586–590. https://doi.org/10.1130/G46218.1.

Mancini, E.A., Llinás, J.C., Parcell, W.C., Aurell, M., Bádenas, B., Leinfelder, R.R., Benson, D.J., 2004. Upper Jurassic thrombolite reservoir play, northeastern Gulf of Mexico. AAPG Bulletin 88, 1573–1602. https://doi.org/10.1306/06210404017.

Mclennan, S.M., 2018. Rare earth elements in sedimentary rocks: influence of provenance and sedimentary processes. In: Geochemistry and mineralogy of rare earth elements. De Gruyter, pp. 169–200.

Mei, M., 2007. Revised classification of microbial carbonates: complementing the classification of limestones. Earth Sci. Front. 14, 222–232. https://doi.org/10.1016/S1872-5791(07)60044-X.

Meng, F., Ni, P., Schiffbauer, J.D., Yuan, X., Zhou, C., Wang, Y., Xia, M., 2011. Ediacaran seawater temperature: evidence from inclusions of Sinian halite. Precambr. Res. 184, 63–69. https://doi.org/10.1016/j.precamres.2010.10.004.

Merdith, A.S., Collins, A.S., Williams, S.E., Pisarevsky, S., Foden, J.D., Archibald, D.B., Blades, M.L., Alessio, B.L., Armistead, S., Plavsa, D., Clark, C., Müller, R.D., 2017. Extending full-plate tectonic models into deep time: linking the Neoproterozoic and the Phanerozoic. Gondw. Res. 50, 84–134. https://doi.org/10.1016/j.gr.2017.04.001.

Meyer, E.E., Quicksall, A.N., Landis, J.D., Link, P.K., Bostick, B.C., 2012. Trace and rare earth elemental investigation of a Sturtian cap carbonate, Pocatello, Idaho: evidence for ocean redox conditions before and during carbonate deposition. Precambr. Res. 192–195, 89–106. https://doi.org/10.1016/j.precamres.2011.09.015.

Miao, M., Sun, Z., Xue, Z., Miao, M., Jiang, K., Zhang, X., Bai, Z., Lyu, X., Zhou, X., Gao, Y., Han, M., Yang, Y., 2024. The lower Cambrian Xiaoerbulake Formation in the Tarim Basin as a potential carbonate source rock. Energy Geosci. 5, 100238. https://doi.org/10.1016/j.engeos.2023.100238.

Michard, A., Albarède, F., Michard, G., Minster, J.F., Charlou, J.L., 1983. Rare-earth elements and uranium in high-temperature solutions from East Pacific rise hydrothermal vent field (13 °N). Nature 303, 795–797. https://doi.org/10.1038/303795a0.

Moffett, J.W., 1990. Microbially mediated cerium oxidation in sea water. Nature 345, 421–423. https://doi.org/10.1038/345421a0.

Oka, A., Tazoe, H., Obata, H., 2021. Simulation of global distribution of rare earth elements in the ocean using an ocean general circulation model. J. Oceanogr. 77, 413–430. https://doi.org/10.1007/s10872-021-00600-x.

Palmer, M.R., Elderfield, H., 1985. Sr isotope composition of sea water over the past 75 Myr. Nature 314, 526–528. https://doi.org/10.1038/314526a0.

Paul, A., Lokier, S.W., Sherry, A., Andrade, L.L., Court, W.M., Land, C., Dutton, K.E., Head, I.M., 2021. Erosion-initiated stromatolite and thrombolite formation in a present-day coastal sabkha setting. Sedimentology 68, 382–401. https://doi.org/10.1111/sed.12783.

Petrash, D.A., Bialik, O.M., Bontognali, T.R.R., Vasconcelos, C., Roberts, J.A., McKenzie, J.A., Konhauser, K.O., 2017. Microbially catalyzed dolomite formation: from near-surface to burial. Earth Sci. Rev. 171, 558–582. https://doi.org/10.1016/j.earscirev.2017.06.015.

Qiu, X., Wang, H., Yao, Y., Duan, Y., 2017. High salinity facilitates dolomite precipitation mediated by Haloferax volcanii DS52. Earth Planet. Sci. Lett. 472, 197–205. https://doi.org/10.1016/j.epsl.2017.05.018.

Reid, R.P., Suosaari, E.P., Oehlert, A.M., Pollier, C.G.L., Dupraz, C., 2024. Microbialite Accretion and growth: Lessons from Shark Bay and the Bahamas. Annu. Rev. Mar. Sci. 16, 487–511. https://doi.org/10.1146/annurev-marine-021423-124637.

Riaz, M., Latif, K., Zafar, T., Xiao, E., Ghazi, S., 2022. Morphology and genesis of the Cambrian oncoids in Wuhai Section, Inner Mongolia China. Carbonates Evaporites 37, 4. https://doi.org/10.1007/s13146-021-00750-5.

Riaz, M., Zafar, T., Latif, K., Ghazi, S. and Xiao, E.Z., 2020. Petrographic and rare earth elemental characteristics of Cambrian.

Rimmer, S.M., 2004. Geochemical paleoredox indicators in Devonian–Mississippian black shales, Central Appalachian Basin (USA). Chem. Geol. 206, 373–391. https://doi.org/10.1016/j.chemgeo.2003.12.029.

Robert, F., Chaussidon, M., 2006. A palaeotemperature curve for the Precambrian oceans based on silicon isotopes in cherts. Nature 443, 969–972. https://doi.org/10.1038/nature05239.

Roberts, J.A., Kenward, P.A., Fowle, D.A., Goldstein, R.H., González, L.A., Moore, D.S., 2013. Surface chemistry allows for abiotic precipitation of dolomite at low temperature. PNAS 110, 14540–14545. https://doi.org/10.1073/pnas.1305403110.

Robles-Fernández, A., Areias, C., Daffonchio, D., Vahrenkamp, V., Sánchez-Román, M., 2022. The Role of microorganisms in the nucleation of carbonates, environmental implications and applications. Minerals 12, 1562. https://doi.org/10.3390/min12121562.

Roger, F., Jolivet, M., Malavieille, J., 2010. The tectonic evolution of the Songpan-Garzê (North Tibet) and adjacent areas from Proterozoic to present: a synthesis. J. Asian Earth Sci. 39, 254–269. https://doi.org/10.1016/j.jseaes.2010.03.008.

Schidlowski, M., 1988. A 3,800-million-year isotopic record of life from carbon in sedimentary rocks. Nature 333, 313–318. https://doi.org/10.1038/333313a0.

Schieber, B., 2007. Changes in the seasonal rhythm of two forest communities during secondary succession. Biologia 62, 416–423. https://doi.org/10.2478/s11756-007-0081-9.

Schröder, S., Grotzinger, J.P., Amthor, J.E., Matter, A., 2005. Carbonate deposition and hydrocarbon reservoir development at the Precambrian–Cambrian boundary: the

Ara Group in South Oman. Sed. Geol. 180, 1–28. https://doi.org/10.1016/j.sedgeo.2005.07.002.
Shackleton, N.J., Kennett, J.P., 1976. Paleotemperature history of the Cenozoic and the initiation of Antarctic glaciation; Oxygen and carbon isotope analyses in DSDP sites 277, 279 and 281. Initial Reports of the Dsdp 29. https://doi.org/10.2973/dsdp.proc.29.117.1975.
Shields, G., Stille, P., 2001. Diagenetic constraints on the use of cerium anomalies as palaeoseawater redox proxies: an isotopic and REE study of Cambrian phosphorites. Chem. Geol. 175, 29–48. https://doi.org/10.1016/S0009-2541(00)00362-4.
Shuster, A.M., Wallace, M.W., Van Smeerdijk Hood, A., Jiang, G., 2018. The Tonian Beck Spring Dolomite: Marine dolomitization in a shallow, anoxic sea. Sed. Geol. 368, 83–104. https://doi.org/10.1016/j.sedgeo.2018.03.003.
Smodej, J., Reuning, L., Becker, S., Kukla, P.A., 2019. Micro- and nano-pores in intrasalt, microbialite-dominated carbonate reservoirs, Ara Group, South-Oman salt basin. Mar. Pet. Geol. 104, 389–403. https://doi.org/10.1016/j.marpetgeo.2019.03.036.
Song, J.-M., Jin, X., Luo, Z., Liu, S.-G., Liu, S.-B., Ma, X.-Z., Li, Z.-W., Lu, X.-S., Zhao, L.-L., Li, K.-R., Ren, J.-X., Tian, L.-Z., Deng, H.-S., 2024. Depositional model of the Member Deng-2 marginal microbial mound-bank complex of the Dengying Formation in the southwestern Sichuan Basin, SW China: implications for the Ediacaran microbial mound construction and hydrocarbon exploration. Pet. Sci. 21, 806–822. https://doi.org/10.1016/j.petsci.2023.12.005.
Sun, X., Dai, M., Qi, Y., Liu, B., Zheng, W., Xing, Z., Wang, M., Li, D., Fan, Y., 2021. Microbiogenic thrombolites from the Cambrian Miaolingian Series of southern North China Craton. Carbonates Evaporites 36, 52. https://doi.org/10.1007/s13146-021-00717-6.
Tan, L., Liu, H., Chen, K., Ni, H., Zhou, G., Zhang, X., Yan, W., Zhong, Y., Lyu, W., Tan, X., Zhang, K., 2022. Sequence sedimentary evolution and reservoir distribution in the third and fourth members of Sinian Dengying Formation, Gaomo area, Sichuan Basin, SW China. Pet. Explor. Dev. 49, 1004–1018. https://doi.org/10.1016/S1876-3804(22)60328-8.
Tang, X., 2018. Characteristics and environmental significance of the sinian dengying formation oncoids in the Northeastern Sichuan Basin-all Databases. Acta Sedimentol. Sin.
Thomas, T.B., Catling, D.C., 2024. Three-stage formation of cap carbonates after Marinoan snowball glaciation consistent with depositional timescales and geochemistry. Nat. Commun. 15, 7055. https://doi.org/10.1038/s41467-024-51412-8.
Thompson, J.B., Ferris, F.G., 1990. Cyanobacterial precipitation of gypsum, calcite, and magnesite from natural alkaline lake water. Geology 18, 995. https://doi.org/10.1130/0091-7613(1990)018<0995:CPOGCA>2.3.CO;2.
Vandeginste, V., Hocknull, E., Fazeli, H., Ji, Y., 2023. Dolomitisation favoured by Lewis acidic background compounds in saline fluids. Environ. Earth Sci. 82, 505. https://doi.org/10.1007/s12665-023-11180-y.
Vasconcelos, C., McKenzie, J.A., Bernasconi, S., Grujic, D., Tiens, A.J., 1995. Microbial mediation as a possible mechanism for natural dolomite formation at low temperatures. Nature 377, 220–222. https://doi.org/10.1038/377220a0.
Wang, J., Gómez, A.H., Pereira, A.G., 2006. Acoustic impulse response for measuring the firmness of mandarin during storage. J. Food Qual. 29, 392–404. https://doi.org/10.1111/j.1745-4557.2006.00081.x.
Wang, J., He, Z., Zhu, D., Liu, Q., Ding, Q., Li, S., Zhang, D., 2020. Petrological and geochemical characteristics of the botryoidal dolomite of Dengying Formation in the Yangtze Craton, South China: constraints on terminal Ediacaran "dolomite seas. Sed. Geol. 406, 105722. https://doi.org/10.1016/j.sedgeo.2020.105722.
Wang, J., Jacobson, A.D., Sageman, B.B., Hurtgen, M.T., 2023. Application of the δ44/40Ca-δ88/86Sr multi-proxy to Namibian Marinoan cap carbonates. Geochim. Cosmochim. Acta 353, 13–27. https://doi.org/10.1016/j.gca.2023.04.023.
Wang, Z., 2014. Paleo-geomorphology formed during Tongwan tectonization in Sichuan Basin and its significance for hydrocarbon accumulation. Petroleum Exploration & Development 41, 338–345. https://doi.org/10.1016/S1876-3804(14)60038-0.
Wang, Z., Jiang, H., Wang, T., Lu, W., Gu, Z., Xu, A., Yang, Y., Xu, Z., 2014. Paleo-geomorphology formed during Tongwan tectonization in Sichuan Basin and its significance for hydrocarbon accumulation. Pet. Explor. Dev. 41, 338–345. https://doi.org/10.1016/S1876-3804(14)60038-0.
Webb, G.E., Kamber, B.S., 2000. Rare earth elements in Holocene reefal microbialites: a new shallow seawater proxy. Geochim. Cosmochim. Acta 64, 1557–1565. https://doi.org/10.1016/S0016-7037(99)00400-7.
Williams, G.E., Schmidt, P.W., 2018. Shuram–Wonoka carbon isotope excursion: Ediacaran revolution in the world ocean's meridional overturning circulation. Geosci. Front. 9, 391–402. https://doi.org/10.1016/j.gsf.2017.11.006.
Williams, J.J., Mills, B.J.W., Lenton, T.M., 2019. A tectonically driven Ediacaran oxygenation event. Nat. Commun. 10, 2690. https://doi.org/10.1038/s41467-019-10286-x.
Wood, R., Bowyer, F., Penny, A., Poulton, S.W., 2018. Did anoxia terminate Ediacaran benthic communities? Evidence from early diagenesis. Precambr. Res. 313, 134–147. https://doi.org/10.1016/j.precamres.2018.05.011.
Wood, R., Bowyer, F.T., Alexander, R., Yilales, M., Uahengo, C.-I., Kaputuaza, K., Ndeunyema, J., Curtis, A., 2023. New Ediacaran biota from the oldest Nama Group, Namibia (Tsaus Mountains), and re-definition of the Nama Assemblage. Geol. Mag. 160, 1673–1686. https://doi.org/10.1017/S0016756823000638.
Wood, R.A., Zhuravlev, A.Y., Sukhov, S.S., Zhu, M., Zhao, F., 2017. Demise of Ediacaran dolomitic seas marks widespread biomineralization on the Siberian Platform. Geology 45, 27–30. https://doi.org/10.1130/G38367.1.
Wu, H.-P., Jiang, S.-Y., Palmer, M.R., Wei, H.-Z., Yang, J.-H., 2019. Positive cerium anomaly in the Doushantuo cap carbonates from the Yangtze platform, South China: Implications for intermediate water column manganous conditions in the aftermath of the Marinoan glaciation. Precambr. Res. 320, 93–110. https://doi.org/10.1016/j.precamres.2018.10.019.
Xiao, C.-T., Wei, G.-Q., Song, Z.-Y., Xiao, Y.-P., Yang, W., Dong, M., Huang, Y.-F., Gao, D., 2019. Petrography and origin of the lower Ordovician microbial carbonates in the Songzi Area of Hubei Province, middle Yangtze region China. Pet. Sci. 16, 956–971. https://doi.org/10.1007/s12182-019-0346-2.
Xiao, E., Zafar, T., Latif, K., Riaz, M., Lu, Y., 2020a. Geochemical and Petrographic analyses of the Cambrian Oncoids of the North China Platform: implications for their Paleogeography and Paleoenvironment. Arab. J. Sci. Eng. 45, 307–325. https://doi.org/10.1007/s13369-019-04146-5.
Xiao, E.-Z., Mei, M.-X., Jiang, S., Zafar, T., 2020b. Morphology and features of Cambrian oncoids and responses to palaeogeography of the North China Platform. J. Palaeogeogr. 9, 7. https://doi.org/10.1186/s42501-020-0055-1.
Yan, H., He, D., Jia, A., Li, Z., Guo, J., Peng, X., Meng, F., Li, X., Zhu, Z., Deng, H., Xia, Q., Zheng, G., Yang, S., Shi, X., 2022. Characteristics and development model of karst reservoirs in the fourth member of Sinian Dengying Formation in central Sichuan Basin, SW China. Pet. Explor. Dev. 49, 810–823. https://doi.org/10.1016/S1876-3804(22)60312-4.
Yao, J., Shu, L., Santosh, M., 2011. Detrital zircon U–Pb geochronology, Hf-isotopes and geochemistry—New clues for the Precambrian crustal evolution of Cathaysia Block, South China. Gondw. Res. 20, 553–567. https://doi.org/10.1016/j.gr.2011.01.005.
Yu, J.-H., O'Reilly, S.Y., Wang, L., Griffin, W.L., Zhang, M., Wang, R., Jiang, S., Shu, L., 2008. Where was South China in the Rodinia supercontinent?: Evidence from U–Pb geochronology and Hf isotopes of detrital zircons. Precambr. Res. 164, 1–15. https://doi.org/10.1016/j.precamres.2008.03.002.
Yuan, Y., Shi, X., Tang, D., Shi, Q., Li, Y., 2022. Microfabrics and organominerals as indicator of microbial dolomite in deep time: an example from the Mesoproterozoic of North China. Precambr. Res. 382, 106881. https://doi.org/10.1016/j.precamres.2022.106881.
Zhai, X., Luo, P., Gu, Z., Jiang, H., Zhang, B., Wang, Z., Wang, T., Wu, S., 2020. Microbial mineralization of botryoidal laminations in the Upper Ediacaran dolostones, Western Yangtze Platform, SW China. J. Asian Earth Sci. 195, 104334. https://doi.org/10.1016/j.jseaes.2020.104334.
Zhang, J., Zhang, B., Shan, X., 2014. Controlling effects of paleo-climate and paleo-ocean on formation of carbonate reservoirs. Pet. Explor. Dev. 41, 135–143. https://doi.org/10.1016/S1876-3804(14)60016-1.
Zhang, P., Huang, K.-J., Luo, M., Cai, Y., Bao, Z., 2022a. Constraining the terminal Ediacaran seawater chemistry by Mg isotopes in dolostones from the Yangtze Platform South China. Precambrian Research 377, 106700. https://doi.org/10.1016/j.precamres.2022.106700.
Zhang, X., Zhou, G., Zhang, P., He, Y., Wei, Z., Wang, G., Zhang, T., He, W., Ma, H., Zhu, C., Wei, J., Ma, X., Yu, X., Li, S., Li, L., Wang, Y., 2022b. Strontium isotope and element constraints on the paleoenvironment of the latest Ediacaran in the Sichuan Basin, southeastern Tibetan Plateau. Front. Earth Sci. 10, 865709. https://doi.org/10.3389/feart.2022.865709.
Zhang, Z., Zhao, L., Zhang, D., Li, Q., Xie, J., Wen, L., Zhang, B., Zhou, G., Zhong, Y., 2024. Formation mechanism of deep to ultra-deep carbonate reservoir: a case study of the Ediacaran Dengying Formation, Penglai area, Sichuan Basin. Aust. J. Earth Sci. 71, 875–896. https://doi.org/10.1080/08120099.2024.2388591.
Zhou, J., Zhang, J., Deng, H., Chen, Y., Luo, X., 2017. Lithofacies paleogeography and sedimentary model of Sinian Dengying Fm in the Sichuan Basin. Nat. Gas Ind. https://doi.org/10.1016/j.ngib.2017.07.023.
Zhou, Z., Wang, X., Yin, G., Yuan, S., Zeng, S., 2016. Characteristics and genesis of the (Sinian) Dengying Formation reservoir in Central Sichuan China. Journal of Natural Gas Science and Engineering. https://doi.org/10.1016/j.jngse.2015.12.005.
Zhu, D., Liu, Q., He, Z., Ding, Q., Wang, J., 2020. Early development and late preservation of porosity linked to presence of hydrocarbons in Precambrian microbialite gas reservoirs within the Sichuan Basin, southern China. Precambr. Res. 342, 105694. https://doi.org/10.1016/j.precamres.2020.105694.
Zhu, T., Dittrich, M., 2016. Carbonate precipitation through microbial activities in natural environment, and their potential in biotechnology: a review. Front. Bioeng. Biotechnol. 4. https://doi.org/10.3389/fbioe.2016.00004.